

LA-4176-TR

DOC. REPORT COLLECTION  
REPRODUCTION  
COPY

LOS ALAMOS SCIENTIFIC LABORATORY  
of the  
University of California  
LOS ALAMOS • NEW MEXICO

Investigation of Mass and Time Distribution  
of Delayed Neutrons in the Thermal Fission  
of  $^{235}\text{U}$  by an On-Line Mass Separator



UNITED STATES  
ATOMIC ENERGY COMMISSION  
CONTRACT W-7405-ENG-36

## LEGAL NOTICE

This report was prepared as an account of Government sponsored work. Neither the United States, nor the Commission, nor any person acting on behalf of the Commission:

A. Makes any warranty or representation, expressed or implied, with respect to the accuracy, completeness, or usefulness of the information contained in this report, or that the use of any information, apparatus, method, or process disclosed in this report may not infringe privately owned rights; or

B. Assumes any liabilities with respect to the use of, or for damages resulting from the use of any information, apparatus, method, or process disclosed in this report.

As used in the above, person acting on behalf of the Commission includes any employee or contractor of the Commission, or employee of such contractor, to the extent that such employee or contractor of the Commission, or employee of such contractor prepares, disseminates, or provides access to, any information pursuant to his employment or contract with the Commission, or his employment with such contractor.

This translation has been prepared in response to a specific request; it is being given standard distribution because of its relevance to the nuclear energy program. Reasonable effort has been made to ensure accuracy but no guarantee is offered.

Printed in the United States of America. Available from  
Clearinghouse for Federal Scientific and Technical Information  
National Bureau of Standards, U. S. Department of Commerce  
Springfield, Virginia 22151

Price: Printed Copy \$3.00; Microfiche \$0.65

**LOS ALAMOS SCIENTIFIC LABORATORY**  
of the  
**University of California**  
LOS ALAMOS • NEW MEXICO

Investigation of Mass and Time Distribution  
of Delayed Neutrons in the Thermal Fission  
of  $^{235}\text{U}$  by an On-Line Mass Separator

by

E. Roeckl

Source: Nuclear Research Center, Jülich, West Germany, Department of Solid-State Physics  
and Neutron Physics, July 1968.

Translated by

Kanner Associates



## CONTENTS

	Page
ABSTRACT .....	1
1. INTRODUCTION .....	1
2. THE MASS SEPARATOR .....	2
2.1 Operating Principle .....	2
2.2 Design .....	3
2.3 Mass Calibration .....	3
2.4 Fission Rate at the Focal Point .....	5
3. NEUTRON-ACTIVITY INVESTIGATION METHODS .....	9
3.1 Activity Buildup .....	9
3.2 Activity Damping .....	10
3.3 n- $\beta$ Coincidence .....	12
3.4 Electronic Equipment and Control .....	13
4. MEASUREMENT .....	14
4.1 Buildup Measurement .....	14
4.2 Damping Measurement .....	16
5. RESULTS AND DISCUSSION .....	17
5.1 Measurement Evaluation .....	17
5.2 Comparison with Known Neutron Emitters .....	22
5.3 Systematics of Delayed Neutron Emission .....	33
6. POSSIBILITIES FOR IMPROVEMENT OF THE METHOD .....	36
SUMMARY .....	36
ACKNOWLEDGMENTS .....	37
REFERENCES .....	37
APPENDIX: CONVOLUTION OF MASS-YIELD DISTRIBUTION .....	38

INVESTIGATION OF MASS AND TIME DISTRIBUTION OF DELAYED NEUTRONS  
IN THE THERMAL FISSION OF  $^{235}\text{U}$  BY AN ON-LINE MASS SEPARATOR

by

E. Roeckl

ABSTRACT

The delayed neutron emission in the thermal fission of  $^{235}\text{U}$  was investigated with a helium-filled mass separator. The neutron activity was measured in coincidence with the  $\beta$  decay arising from neutron emission. From the measurement of the activity buildup, the neutron yield for various times after fission was determined, and the half-life was obtained from the measurement of the activity decay. The mass distribution of these magnitudes was determined in the total fission yield range. The total neutron yield of light fission products is 1.05 neutrons/100 fissions, and that of heavy fission products is only 0.53 neutrons/100 fissions. The measured mass and time dependence was compared with the previously published values for identified neutron emitters. Previously unidentified fractions of the activity in the mass range from 85 to 88 (half-life of 1 sec) and the mass range from 96 to 100 (half-life of 1.5 sec) are discussed. The yield variation between light and heavy fission products is indicated on the basis of the systematics of the delayed neutron emission, and the previously unidentified activity was assigned to the mother nuclides  $^{98}\text{Y}$  and  $^{99}\text{Y}$ .

1. INTRODUCTION

Since Roberts, Meyer, and Wang<sup>1</sup> discovered the delayed emission of neutrons in nuclear fission, in 1959, this theoretically and practically interesting phenomenon has been the subject of numerous investigations. Study of this rare type of radioactive disintegration contributes to understanding of the disintegration mechanism, of the structure of neutron-rich nuclei, and of the energy-mass trough and provides data for design of particular reactor types.<sup>2</sup>

Delayed neutron emission is possible during  $\beta$  decay of a fission product (parent nuclide) when the state of excitation in the daughter nucleus exceeds the neutron binding energy of the daughter nucleus (neutron emitter). The half-life of neutron emission is that of the preceding  $\beta$  disintegration. The decay of delayed neutron activity was measured for numerous fission processes, and classified into six groups characterized by average half-lives of 55, 22, 5.4, 2.3, 0.51, and 0.19 sec. Although relative and absolute yields of

these groups differ substantially from one fission process to another, the average half-lives remain approximately equal.<sup>3</sup> The contributions of individual neutron emitters to these half-life groups are not yet adequately known.

Radiochemical separation methods have been successfully used to identify delayed neutron emitters and to determine their yield.<sup>4-10</sup> Basic difficulties in these methods are limited separation speed, differentiation of chemically related elements, and mass correlation within an isotope series. These problems can be solved by using on-line separators to study delayed neutrons; the separation time is negligibly small compared to the half-lives, and mass correlation is unambiguous.

On-line mass separators that combine rapid radiochemical separation and separation by a magnetic field have been developed.<sup>10-12</sup> In contrast to these separators, a helium-filled on-line mass separator can separate a beam of chemically non-preserved fission products according to mass. Use

of this apparatus to study delayed neutron emission was proposed by Cohen and Fulmer<sup>13</sup> as early as 1958.

This report presents measurements of time and mass distribution of delayed neutron emission in  $^{235}\text{U}$  fission performed with the helium-filled mass separator of the Jülich FRJ-2 research reactor.

## 2. THE MASS SEPARATOR

### 2.1. Operating Principle.

Charged particles are deflected in a magnetic field,  $B$ , in accordance with the expression

$$B\rho \sim \frac{Av}{q} \quad (1)$$

where

- $\rho$  = the ion path's radius of curvature in the magnetic field,
- $A$  = ion mass number,
- $v$  = ion velocity, and
- $q$  = ion charge number.

Let the deflection path along the magnetic field be filled with gas. The ion charges change through collision with the gas atoms. A single ion's deflection in the magnetic field is then proportional to the average charge,  $\bar{q}_1$ , of all ionic charge states that this ion assumed on its path through the field. With a high enough number of impacts,  $\bar{q}_1$  becomes equal to the average ion charge number,  $\bar{q}$ , of all ions of equal mass and nuclear charge in the gas. The average ion charge,  $\bar{q}$ , of heavy ions passing through matter may be described by the following empirical relationship given by Heckman et al.<sup>14</sup> and confirmed by Betz et al.<sup>15</sup>

$$\bar{q}(v, Z) = Z \left[ 1 - C \exp \left( -\frac{v}{v_0 Z^Y} \right) \right] \quad (2)$$

where

$Z$  = atomic number of the ion, and

$v_0 = \frac{c}{137}$  ( $c$  = velocity of light).

$C$  and  $Y$  are parameters that are independent of velocity and vary only slowly with the atomic number,  $Z$ , of the ion and with the nuclear charge of the moderator.  $C = 1$ , and  $Y = 2/3$  yields for  $v < v_0 Z^Y$  the general relationship postulated by Bohr<sup>16</sup> for  $\frac{v}{v_0} > 1$ :

$$\bar{q}(v, Z) = \frac{v}{v_0} Z^{1/3} \quad (3)$$

Substitution of this expression for the ion charge,  $q$ , in Eq. (1) shows that  $B\rho$  is independent of  $v$ . Grueter's measurements<sup>17</sup> of  $^{94}\text{Sr}$  ions from the mass separator beam using helium as the charge-transfer gas have shown, however, that  $C$  and  $Y$  deviate from the values assumed in Eq. (3). Nevertheless, deflection in the magnetic field is independent of the fission product velocity and of its ionic-charge states over a wide range of velocities. One may therefore use relatively thick fission sources that have a greater spread than the ( $\frac{\Delta v}{v}$  FWHM = 6.5%) initially present in fission. The thick fission source and the deflection's independence of the ion-charge state give the high radiation intensity that is the helium-filled mass separator's most important advantage.

Equation (2) applies to the average fission-product ion-charge number,  $\bar{q}$ . Despite the large breadth of the ion-charge distribution ( $\frac{\Delta q}{q}$  FWHM = 25%) originally present in fission, mass separation with fair resolution becomes possible because of the gas-filling of the deflection path. The following fission-product interactions with the gas must be taken into account: changes in the ion-charge state caused by charge-altering collisions, changes in the flight direction caused by elastic nuclear collisions, and energy decrease by ionization, i.e., by interaction with the electrons of the gas atoms. The ion-charge distribution,  $q_1$ , averaged over the path in the magnetic field becomes narrower as the charge-altering collisions increase; i.e., resolution increases with increasing gas pressure. On the other hand, spreading of the beam by multiple scattering increases as the number of collisions and energy loss increase; i.e., resolution decreases with increasing gas pressure. Because of this combination of processes, resolution expressed as a function of gas pressure passes through a minimum. This pressure functionality remains even if all other effects on resolution are taken into account. Of the various light gases, helium has provided the best  $B\rho$  resolution obtained so far.<sup>17</sup>

### 2.2. Design.

A helium-filled mass separator operating on the principle outlined by, and similar to those built by, Cohen and Fulmer<sup>13</sup> in 1958 at Oak Ridge, and Armbruster<sup>18</sup> in 1961 at Munich, is now operated

at the Jülich (FRJ-2) research reactor.<sup>19</sup> Figure 1 shows the separator layout; Fig. 2 shows the installations outside the biological shield viewed from the top of the reactor.

A layer of  $^{235}\text{U}$  ( $1 \text{ mg/cm}^2$ ) at the hot end of the radiation tube in a  $10^{14}/\text{cm}^2\text{-sec}$  thermal-neutron flux provides a source strength of  $5 \cdot 10^{12}$  fission products/sec. Fission products falling into the solid angle of the evacuated (1.4 Torr) radiation-tube collimator enter a magnetic deflection system and are separated outside the biological shield from the neutron and  $\gamma$ -radiation absorbed in the beam catcher. The stigmatic focusing deflection system which deflects the fission product beam by  $33^\circ$  consists of two magnets with alternating field gradient. Thin VYNS foil ( $70\text{-}\mu\text{g/cm}^2$ ) separates the helium sector in the magnetic field from the vacuum components of the apparatus.

The detector assembly suitable for a particular study is set up at the focal point of the deflection system. The intensity of the fission-product radiation beam separated according to mass at the focal point is  $10^{14}/\text{cm}^2\text{-sec}$  for high-yield fission products. Fission-product flight time from source to focal point, and thus the delay time compared to the fission event, is  $1 \mu\text{sec}$ .

### 2.3. Mass Calibration.

Mass calibration of the separator, i.e., correlation of the  $B_0$  value and fission-product mass,  $A$ , according to Eq. (1), is performed experimentally using long-lived fission products that can be identified by their known half-lives and the energy of pronounced  $\gamma$  lines. The method<sup>20, 21</sup> is similar to the decay method described in Sec. 3.2. In the mass separator, the  $B_0$  range of interest is covered by changing the magnetic field,  $B$ , at a constant radius of curvature fixed by the ion optics of the apparatus.

The intensity of a known  $\gamma$  line as a function of  $B$  to 1/10 of its maximum can be described by a Gaussian curve:

$$f(B) = \frac{1}{\sigma\sqrt{2\pi}} \exp \left[ -(B - B_0)^2 / 2\sigma^2 \right] \quad (4)$$

The center of mass,  $B_0$ , of the line configuration,  $f(B)$ , is attributed to the mass,  $A_1$ , of the emitting nuclide; its spread is a measure of the separator's resolution capacity. The relationship of

standard deviation,  $\sigma(B)$ , and relative FWHM  $(\frac{\Delta B}{B})_{\text{FWHM}}$  is

$$\sigma(B) = \frac{B}{2\sqrt{2\ln 2}} \left( \frac{\Delta B}{B} \right)_{\text{FWHM}} \quad (5)$$

The relative FWHM  $(\frac{\Delta B}{B})_{\text{FWHM}}$  of the Gaussian curve was measured for various light gases as a function of the pressure in the charge-transfer chamber. Optimum operating conditions, i.e., optimum resolution capacity, for light fission products was attained with helium pressure of 6.7-mm Hg.<sup>19</sup> Both mass calibration and all measurements of light fission products were made under these conditions.

The relative  $(\frac{\Delta B}{B})_{\text{FWHM}}$  on the mass scale can be computed from the measured  $B_0$ -resolution capacity:

$$\left( \frac{\Delta A}{A} \right)_{\text{FWHM}} = \frac{\Lambda}{\Gamma(A)} \left( \frac{\Delta B}{B} \right)_{\text{FWHM}} \quad (6)$$

where  $\Gamma$  is the mass dispersion,

$$\Gamma(A) = \frac{dB/B}{dA/A} \quad (7)$$

Figure 3 summarizes the separator characteristics for light fission products as a function of mass. The mass-calibration curve, (a), Fig. 3, was determined by a computer program that computes one mass-dispersion value, (b), Fig. 3, from each five neighboring calibration points. The relative  $B_0$ -resolution measurement gives a constant value of 4.3% for the entire mass range. The straight line, (c), Fig. 3 is the result of a computer fit assuming linear behavior. (d), Fig. 3 shows the relative mass-resolution capacity computed by Eq. (7).

The best heavy fission-product resolution was obtained with 4.4-mm Hg helium pressure. Figure 4 summarizes the characteristic data for these operating conditions at which all heavy fission-product measurements were performed. Here the relative  $B_0$ -resolution capacity is 6.1%. Combined with the appreciably poorer mass dispersion for heavy fission products, this gives a mass-resolution capacity about three times poorer than that for light fission products.

In using the mass-calibration curve, one must remember that the mass separator has nuclear charge dispersion as well as mass dispersion, in accordance with Eq. (2). The long-lived nuclides used for calibration are produced cumulatively by  $\beta$  disint-

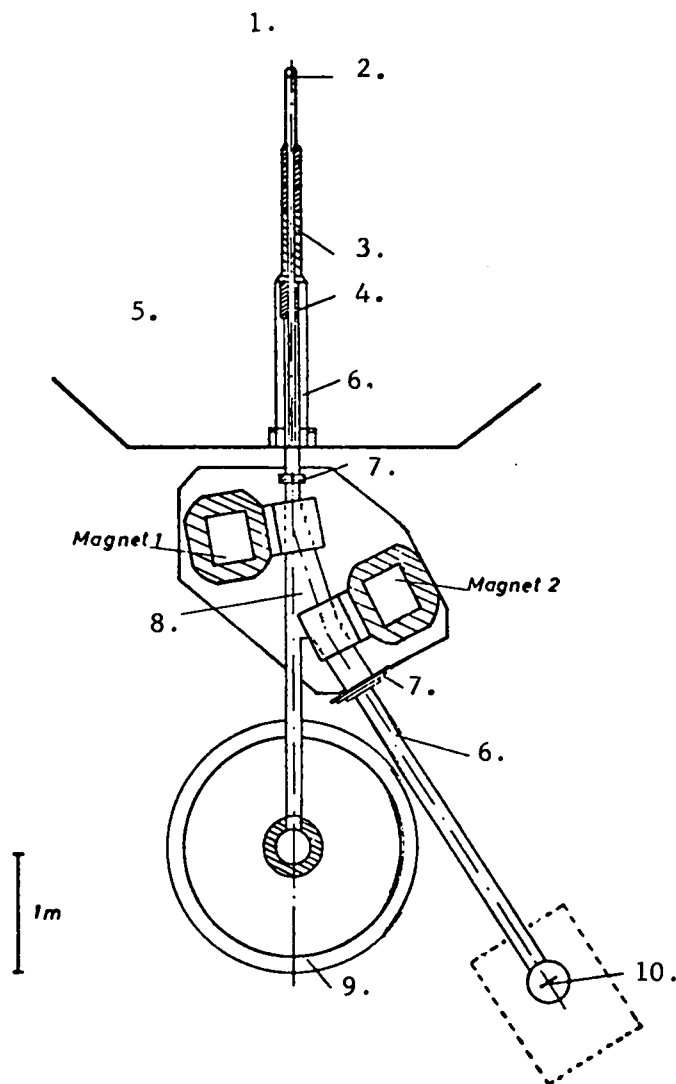


Fig. 1. Layout of helium-filled mass separator.

- |                                    |  |
|------------------------------------|--|
| 1. Reactor core                    | 6. Vacuum  |
| 2. $^{235}\text{U}$ fission source | 7. VYNS window   |
| 3. Collimator                      | 8. Charge-transfer chamber, $\sim 1\text{-mm Hg}$ helium |
| 4. Shutoff                         | 9. Beam catcher  |
| 5. Biologic shield                 | 10. Image plane  |

tegration of short-lived parents rather than primarily in fission. Separation in the mass separator occurs in short times compared to the  $\beta$ -disintegration half-life. The atomic number applicable to the calibration nuclides, which according to Eq. (2) affects the deflection in the magnetic field, is therefore not their own nuclear charge, but rather the center of mass,  $Z_p(A)$ , of the primary nuclear charge distribution in the mass chain,  $A$ . The mass calibration curve shown in Figs. 3 and 4 (a) applies to all fission products not produced by primary fission. However, the deflection of a

primary fission product is governed by the average atomic numbers of the parents including the nuclide being studied. Let this average be smaller than  $Z_p$  by  $\Delta Z$ . As shown explicitly in Ref. 20, the corresponding mass dislocation,  $\Delta A$ , of a nuclide of mass  $A$  and nuclear charge  $Z$  is

$$\Delta A = \frac{\Gamma(A) - 1}{\Gamma(A)} \cdot \frac{A}{Z} \cdot \Delta Z \quad (8)$$

Since  $\Delta Z \leq 0$  and  $\frac{\Gamma(A)}{\Gamma} \leq 0$ , we have  $\Delta A \geq 0$ ; i.e., the mass separator indicates excessive mass for primary fission products.

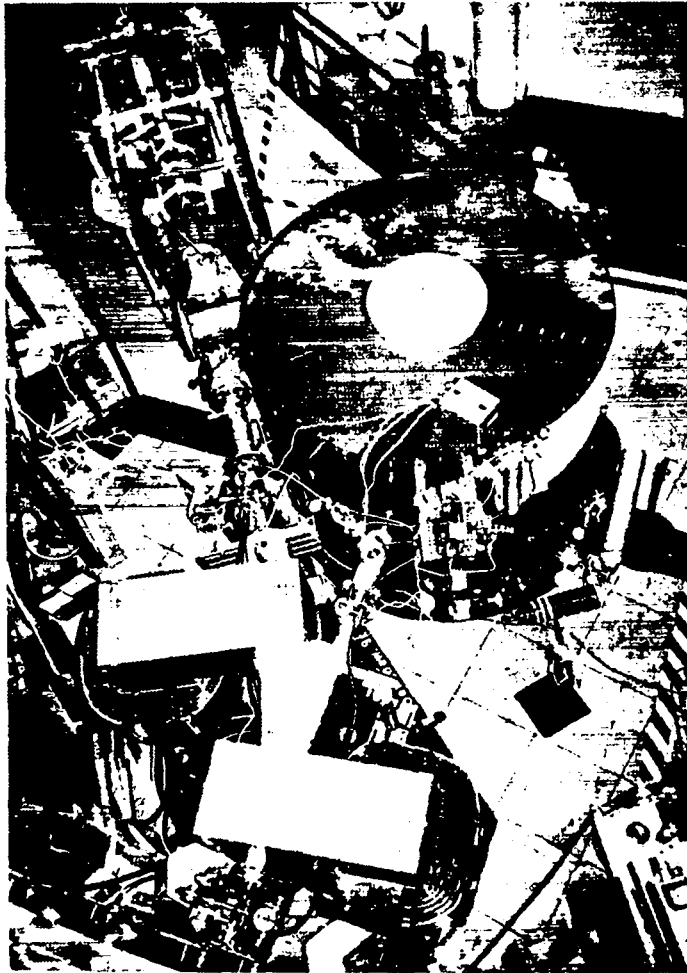


Fig. 2. Mass separator viewed from the top of the reactor.

#### 2.4. Fission Rate at the Focal Point.

The fission rate at the separator focus was recorded as a function of the magnetic field,  $B$ , for the following reasons.

1. Comparison of measured distribution involving convolution of radiochemically determined yield distribution with the apparatus resolution capacity tests the applicability of convolution that will be repeated several times in similar form.

2. Radiation intensity must be known for the tests described below.

The fission rate was measured using a semiconductor detector mounted at the focal point and connected to a charge-sensitive preamplifier (ORTEC). Fission rates were recorded as a function of  $B\rho$  value both at 6.7-Torr helium (optimum pressure for light fission products) and at 1.4-Torr

helium (optimum for heavy fission products). Figure 5 shows uncorrected counting rates at the semiconductor detector as they occurred in testing. Only the straight-line portion of the test curves is used hereafter because calibration is available for these portions (Figs. 3 and 4 (a)).

Figure 5 shows that the separator clearly separates light and heavy fission products. In contrast, the ratio of maximum yield (mass 95) to minimum yield (mass 120), which is  $\sim 600$  for the initial yield distribution, is only 10 for the measured fission-product distribution. The maximum, corresponding to the heavy fission-products, is relatively narrow despite the poor  $B\rho$  resolution because of the low mass dispersion in this mass range (see Fig. 4).

To compare the measured fission-product distribution with the radiochemically measured mass

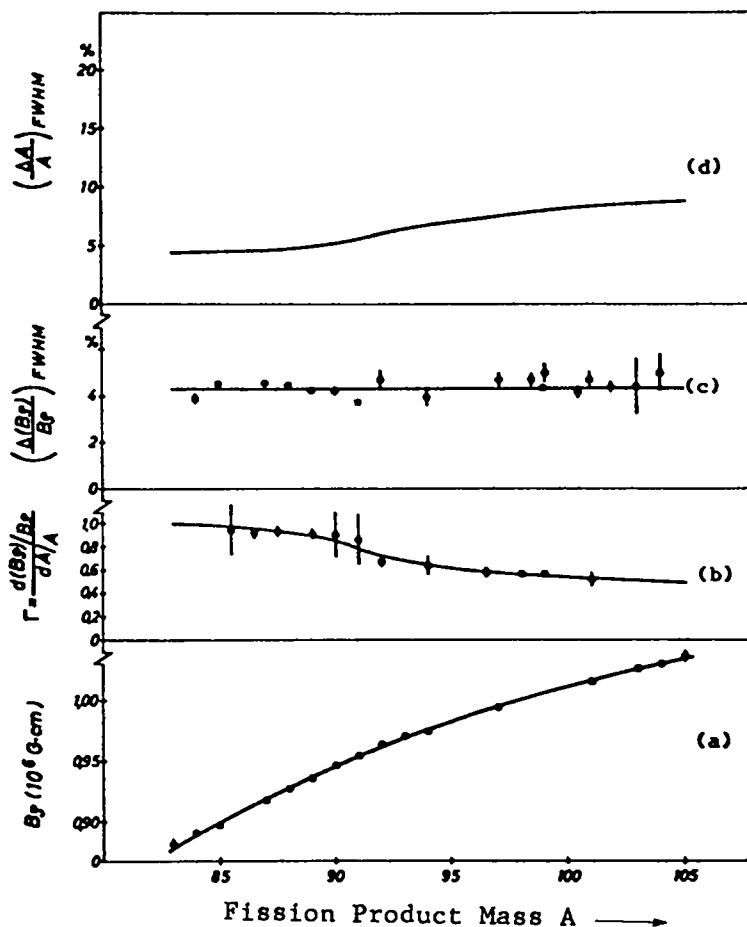


Fig. 3. Typical mass separator data for light fission products.  
 (a) Mass-calibration curve  
 (b) Mass dispersion  
 (c) Bp resolution capacity  
 (d) Mass-resolution capacity

distribution, the convolution of the latter function and the apparatus resolution capacity is formed by taking the mass-calibration curve into account. The convolution was formed by use of a computer program in accordance with Eq. (A7) derived in the Appendix. The radiochemically measured fission-yield values were taken from Farrar et al.<sup>22,23</sup> Convolution according to Eq. (A7) yields a distribution related to a constant detector interval,  $\Delta x_0$ , which can be directly compared to the test curve shown in Fig. 5. However, we will make comparisons using "undistorted" distributions, i.e., distributions related to a constant  $\Delta B$  interval (see Appendix). Figure 6 shows the measured fission rates after 1/B correction as open circles, and the convoluted radiochemical distribution as a continuous curve. In addition to the magnetic field, B, Fig. 6 shows the average

mass,  $\bar{A}$ , i.e., the center of the mass mixture at the focus for a particular B. The values of  $\bar{A}$  were computed according to Eq. (A8). The measured data and computed distributions, which in each instance were fitted to the rates of the maximum, agree well. The dash-dotted lines indicate the ranges wherein agreement is better than 10%. Within these ranges, both mass correlation and comparison with a computed distribution can be considered reliable. The deviations along the legs of the distribution curves, clearly visible in Fig. 6, presumably occur because the configuration is not a pure Gaussian curve as was assumed in forming the convolution. For reasons of ion physics, the configuration may be expected to be unsymmetrical toward larger Bp values. However, this leg of the configuration, which would at least partially explain the deviations, could not be confirmed by  $\gamma$  spectroscopy be-

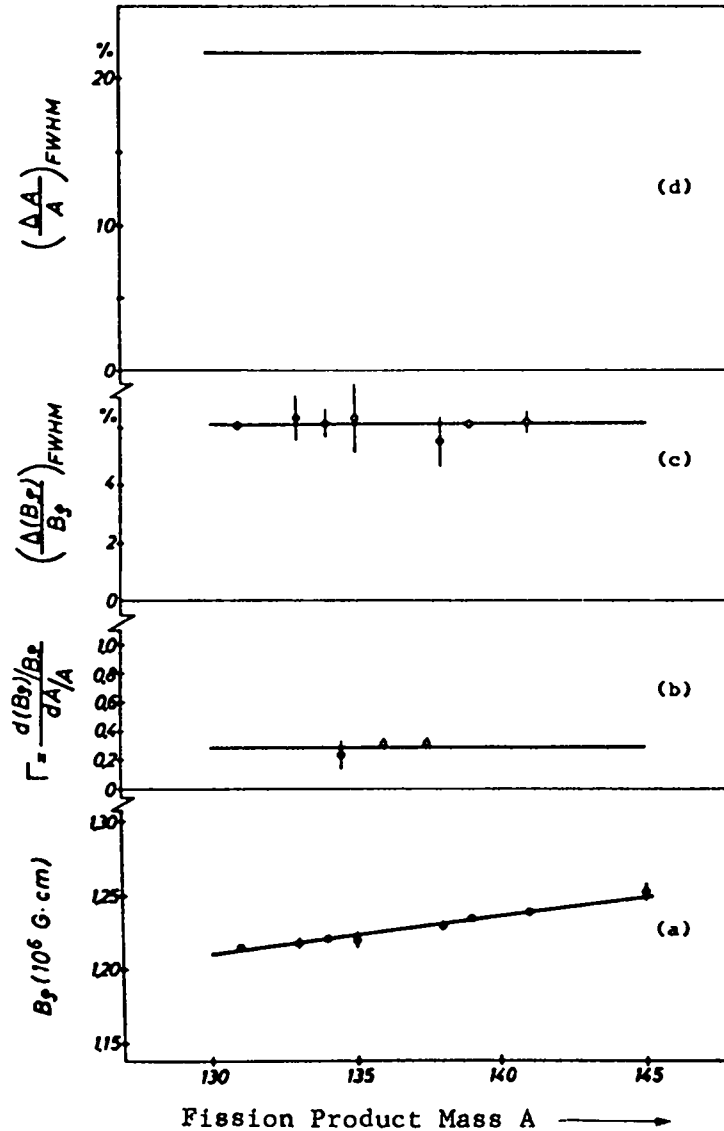


Fig. 4. Typical mass separator data for heavy fission products.  
 (a) Mass-calibration curve  
 (b) Mass dispersion  
 (c) Bp resolution capacity  
 (d) Mass resolution capacity

cause the  $\gamma$  lines at respective distances from their Bp maxima are obscured by the background or by concurrent lines.

The intensity at the focus is less for heavy than for light fission products because of different multiple scattering. This intensity difference can be generally described by a mass-dependent loss factor. However, the convoluted distributions can be made to agree with the test values by one fit that is the same for all light fission products, and by another for all heavy fission products (Fig. 6). It is therefore safe to assume one constant

loss factor for light fission products and another for heavy fission products.

To evaluate the measurements, only the relative fission-rate distribution at the focus, not the absolute rates, need be known as a function of the magnetic field. Using the above assumption about the multiple-scattering loss factor, it is sufficient to determine the intensity ratio,  $k$ , of light and heavy fission products.  $k$  is obtained from the measured fission-product distribution by separate integration of the two mass ranges. We assumed that the two mass ranges are always sepa-

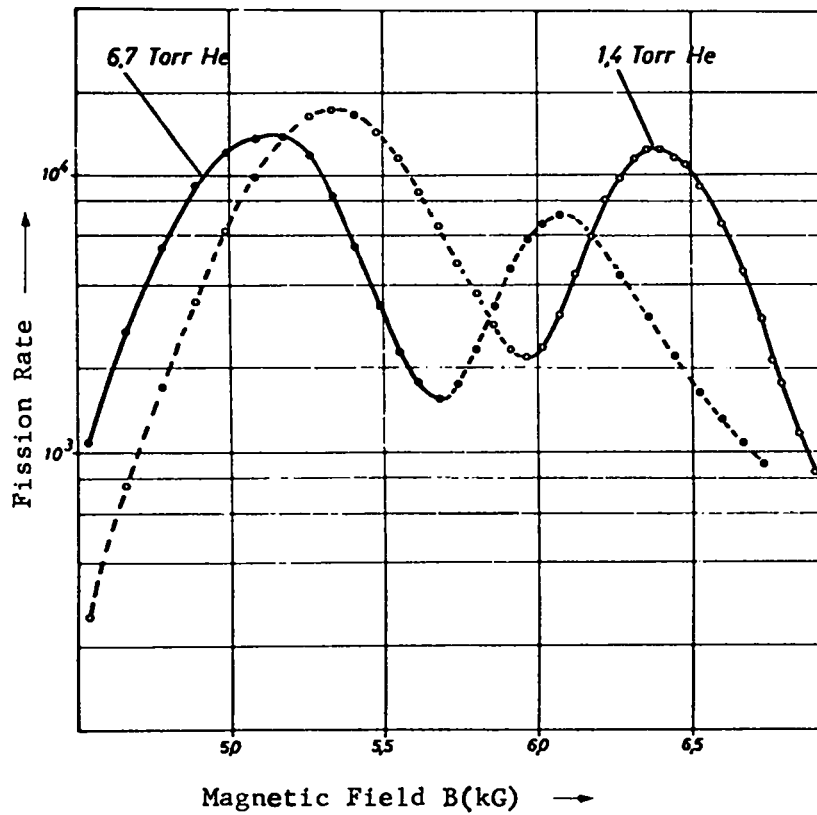


Fig. 5. Fission rate at the separator focus as a function of  $B_0$  value for 1.4- and 6.7-Torr He in the charge-transfer chamber.

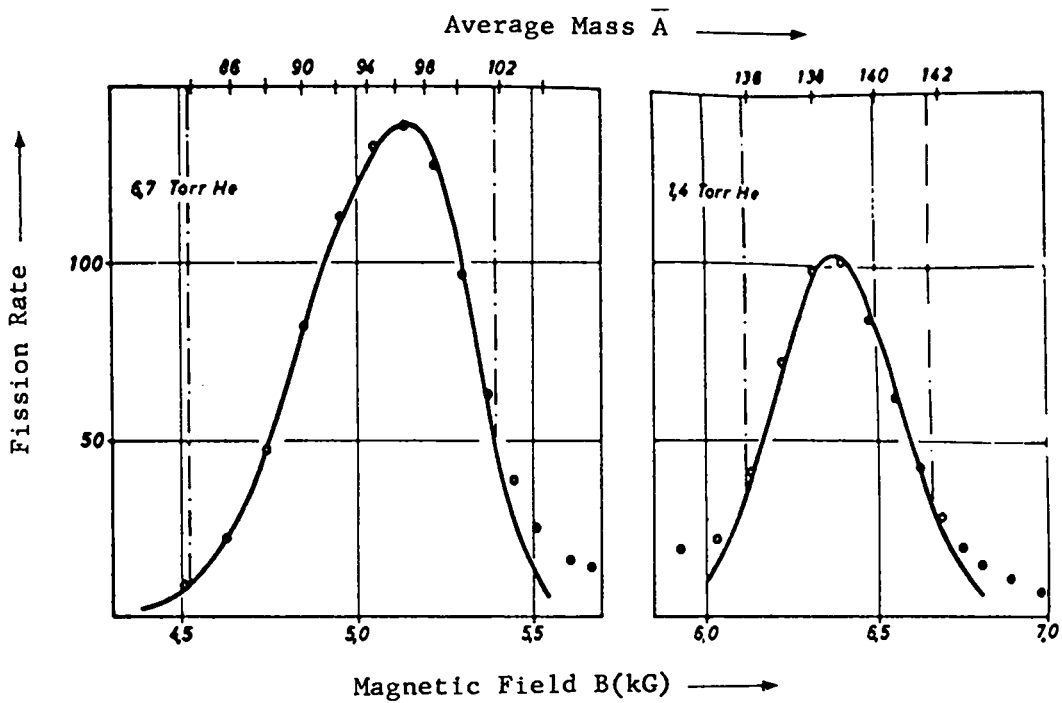


Fig. 6. Comparison of measured (O) and computed (-) fission-product distribution.

rated by the distribution trough. This yields:

$$k = \frac{k_s}{k_e} = \frac{\text{Intensity of Heavy Fission Products} / 1.4 \text{ Torr He}}{\text{Intensity of Light Fission Products} / 6.7 \text{ Torr He}} = 0.61 \quad (9)$$

An attempt to determine the ratio  $k$  by absolute counting of known-energy  $\gamma$  quanta emitted by the fission products yields only inaccurate results. However, the correctness of the measured absolute fission rates,  $k_e$  and  $k_s$ , was checked by a  $\beta$ -chain length measurement<sup>24</sup> in the mass separator. In this measurement, the number of  $\beta$ -particle fissions is determined from the  $\beta$  rate counted in  $4\pi$  geometry and from the fission rate measured by a semiconductor detector. The result agreed well with other authors' values, which may be taken as confirmation of the result of Eq. (9).

### 3. NEUTRON-ACTIVITY INVESTIGATION METHODS

#### 3.1. Activity Buildup.

The activity buildup can be used to determine yields because the separator's separating period is short compared to all  $\beta$ -disintegration half-lives, and because the separation method is continuous. This method, first used by Alzmann,<sup>25</sup> has successfully measured fission-product  $\beta$ -chain lengths.<sup>26</sup>

Let a beam of parent nuclides whose properties are identified by the subscript  $i$  be collected by a foil, with the number,  $s_i$ , of particles impacting per second being constant over time. Let the neutron activity building up in the foil over time be  $r_i(t)$ . At time  $T$  after the start of irradiation, the activity is

$$r_i(T) = s_i \int_0^T n_i(T - t') dt' \quad (10)$$

where  $n_i(T - t')$  is the neutron activity at the instant of observation,  $T$ , of nuclides collected in the foil at time  $t'$  after the start of irradiation. Because of the short flight time of fission products in the separator,  $t'$  also indicates the instant of the corresponding fission process. Introducing  $t = T - t'$  yields

$$r_i(T) = s_i \int_0^T n_i(t) dt \quad (11)$$

The fission rate at the focus is taken as

$$s_i = k_e \cdot Y_c^{(i)} \quad (s) \quad (12)$$

where  $Y_c^{(i)}$  is the cumulative fission yield from the parent nuclide.  $k_e$  and  $k_s$  are factors which from the  $Y_c^{(i)}$  produce the actual intensity of light or heavy fission products at the focus; they are governed by the fission rate at the source, by the solid angle covered by the apparatus, and by the multiple fission-product scattering losses in the charge-transfer chamber and windows.

In Eq. (12), we set

$$\int_0^T n_i(t) dt = P_n^{(i)} \int_0^T v_i(t) dt \quad (13)$$

where  $P_n^{(i)}$  is the branching ratio of neutron and  $\beta$  disintegrations and  $v_i(t)$  describes the time buildup of neutron activity and is normalized to unity.

From Eqs. (12), (13), and (14), it follows that

$$r_i(T) = k_e \cdot P_n^{(i)} \cdot Y_c^{(i)} \cdot \int_0^T v_i(t) dt \quad (s) \quad (14)$$

Without considering the scale factor  $k_e$  or  $k_s$ , the neutron activity at time  $T$  after start of irradiation is the number of neutrons emitted after fission up to time  $T$ .

When the fission-product beam of the mass separator is collected at a known BP value on a foil (breadth  $\Delta X_0$ ) mounted at the focus, a mass mixture is present because of the moderate resolution capacity. Equation (14) is now replaced by a sum for all  $i$  neutron emitters that contribute to activity, convoluted with the separator resolution capacity. The neutron activity per  $\Delta X_0$  interval is found from Eq. (A7) when the fission yields,  $\eta_i$ , mentioned in the Appendix are replaced by

$$P_n^{(i)} Y_c^{(i)} \int_0^T v_i(t) dt.$$

If the irradiation time,  $T$ , is chosen fairly long compared to the half-lives of the parent nuclides that characterize the neutron emission,

$\int_0^T v_i(t) dt$  approaches 1 for all  $i$ . In this case,

the neutron activity is directly proportional to the absolute neutron yield,  $P_n Y_c$ , convoluted with the separator resolution capacity. The time behavior of a particular emitter (which depends on the decay of generally unknown ancestors) no longer enters into the expression.

By measuring this "saturated" neutron activity as a function of  $B\beta$  value and taking into account the different radiation intensities of light and heavy fission products, the integral may be joined over the entire mass range to the well-known absolute value of all delayed neutrons per fission. This amounts to absolute calibration of the detector which need not be operated in  $4\pi$  geometry. For this purpose one need not know the absolute fission rate, only its relative behavior.

Figure 7 shows the experimental apparatus used for buildup measurement. The collimated fission-product beam is released by a fast magnetic shutter (opening period 30 msec) and collected at the separator focus in a thin nylon band which is part of the transport device described in more detail in Sec. 3.2. Increasing  $\beta$  contamination and the associated increased random coincidence background are avoided by always removing the exposed section of the transport band on completion of an exposure.

### 3.2. Activity Damping.

The neutron yields at a specific time after fission, or at saturation, can be obtained from the buildup measurement described in Sec. 3.1. In principle, the buildup curve also contains information on all half-lives present in the mass mixture. However, measurement of activity damping is better suited to half-life analysis of the mass mixture existing at the separator, or to investigating the decay of a particular nuclide. An intermittently operated transport device that is a further development of that described by Hovestadt<sup>10</sup> was used for this purpose.

Figure 8 shows the transport system and detector assembly for damping measurements. In contrast to the apparatus for buildup measurements, irradiation and detector sections are here separate. A  $6\text{-cm}^2$  portion of a 500-m-long nylon band is irradiated for a preselected period and then transported rapidly into the detector section. Transport time, short compared to the irradiation time,  $T_B$ , is a minimum of 0.1 sec. While the decay events of the irradiated part of the band are being registered, the irradiation section is again used for irradiating. The irradiation period,  $T_B$ , is therefore identical to the time available for meas-

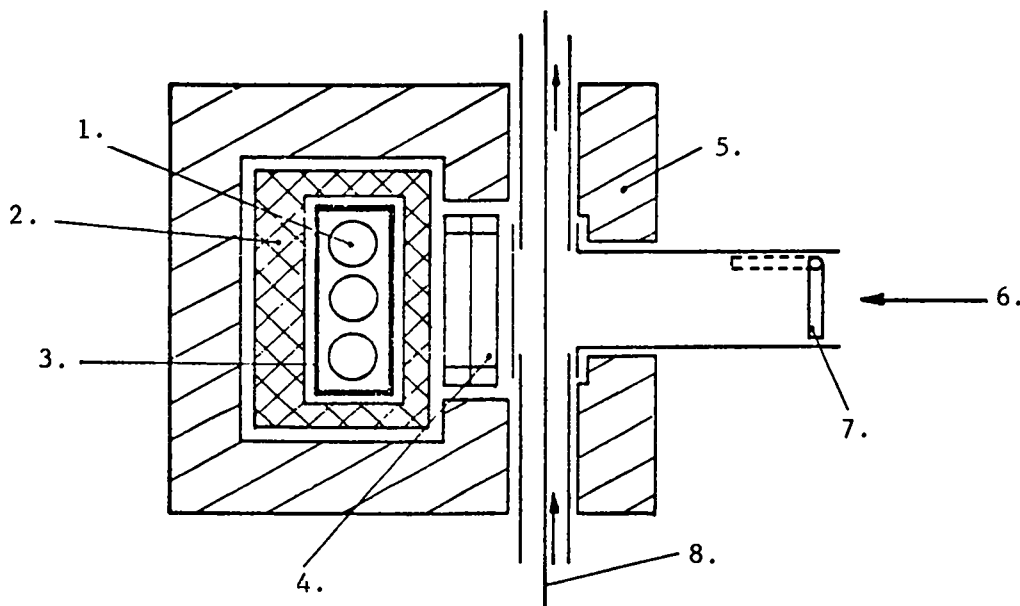


Fig. 7. Experimental apparatus for buildup measurement.

- |   |  |
|---|--|
| 1 - $^3\text{He}$ counter-tube assembly | 5 - Neutron shield                         |
| 2 - Polyethylene                        | 6 - Fission-product beam                   |
| 3 - Cadmium absorber                    | 7 - Fast shutter                           |
| 4 - $\beta$ proportional counter        | 8 - Intermittently operated transport band |

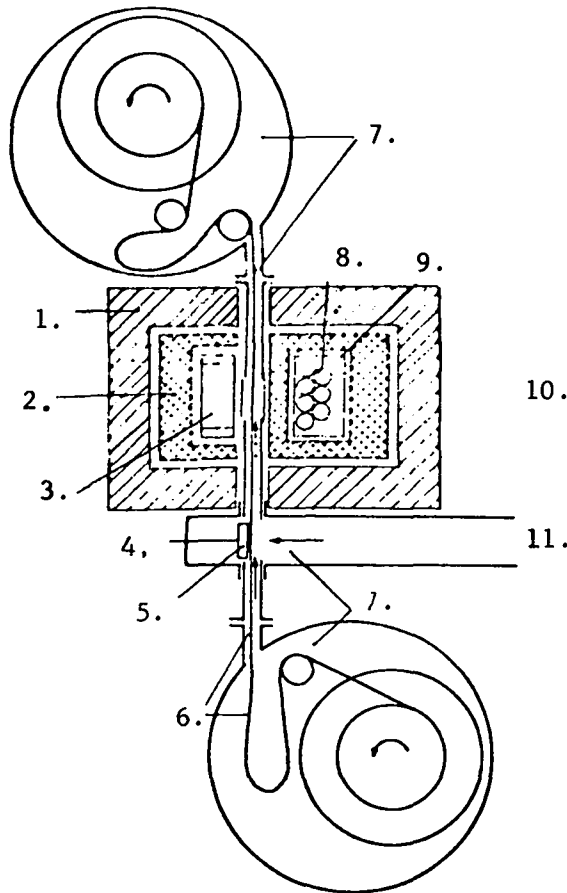


Fig. 8. Transport system and detector assembly for damping measurement.

- |   |  |
|---|--|
| 1 - Compressed wood shield                            | 6 - Intermittently operated transport band |
| 2 - Polyethylene                                      | 7 - Vacuum chamber                         |
| 3 - $\beta$ counter tube                              | 8 - $^3\text{He}$ counter tube bank        |
| 4 - Irradiation position                              | 9 - Cd absorber                            |
| 5 - Fission-product monitor (semi-conductor detector) | 10 - Counting position                     |
|   | 11 - Fission-product beam                  |

urement and is subsequently referred to as the cycle time for the transport device irradiation-measurement cycle.

Activity is measured in the detector section during the time interval  $t_1$  to  $t_2$  ( $0 \leq t_1 \leq t_2 \leq T_B$ ) after termination of irradiation. For a nuclide with the decay constant  $\lambda$ , the amount,  $h$ , of the nuclides applied by irradiation in the irradiation section during time  $T_B$ , which decays in the detector section during the interval  $t_1 - t_2$ , is given by

$$h = \frac{1}{\lambda T_B} (1 - e^{-\lambda T_B}) (e^{-\lambda t_1} - e^{-\lambda t_2}) \quad (15)$$

$$\lambda = \frac{\ln 2}{T_{1/2}}$$

where  $T_{1/2}$  = half-life.

In Eq. (15) we assume that the particular nuclide is exclusively of primary origin, or that the half-lives of all parents are small compared to  $T_{1/2}$ . Figure 9 shows  $h$  plotted as a function of

$$\frac{T_{1/2}}{T_B} \text{ for the special case } t_1 = 0.14 \cdot T_B, t_2 = 0.90 \cdot T_B. \quad h\left(\frac{T_{1/2}}{T_B}\right) \text{ can be considered the time-}$$

resolution function of the intermittent transport system. For a fixed cycle time  $T_B$ , there is preference for a specific half-life ( $T_{1/2}^{(opt)} = 0.6T_B$ ), and both smaller and greater half-lives are suppressed. However, this resolution function is very wide (FWHM =  $4.5 \cdot T_{1/2}^{(opt)}$ ). As shown by

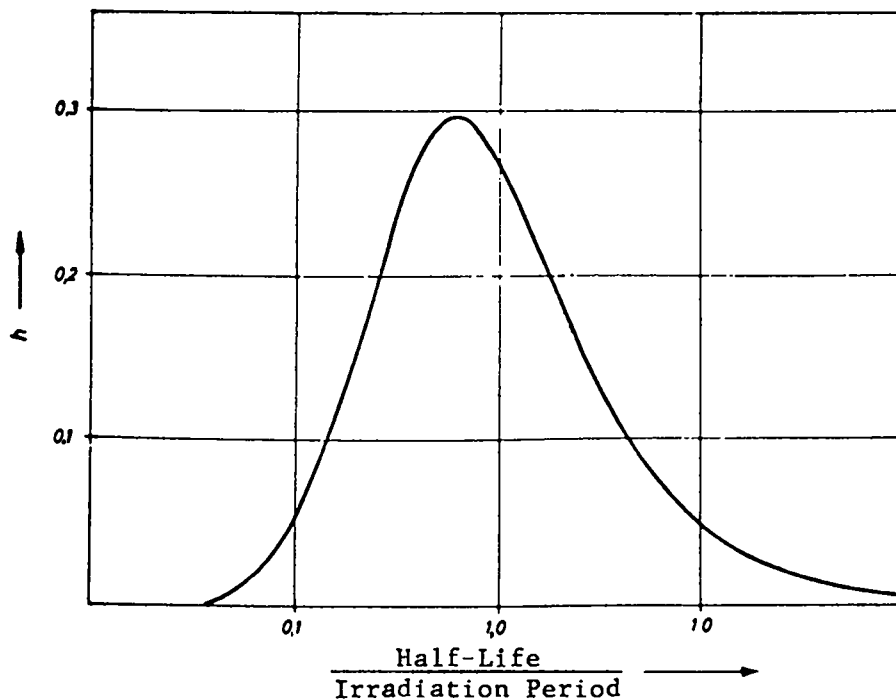


Fig. 9. Time-resolution function of the transport system.

Hovestadt,<sup>27</sup> maximum values of  $h = 40\%$  are obtained for  $t_1 = 0$ ,  $t_2 = T_B$ , i.e., four times greater intensity than is obtainable with a continuously operating transport band.

### 3.3. n- $\beta$ Coincidence.

Delayed neutrons, which have average energies of about 500 keV,<sup>28-30</sup> are slowed down in polyethylene and detected in an assembly of 2-in.-diam. by 4-in.  $^3\text{He}$ -counter tubes (Texlum Corporation). By use of pulse-height discrimination, the neutron detector is made insensitive to  $\gamma$  rays and electrons. By use of a strong  $^{60}\text{Co}$  source, we determined a discriminator setting at which the detector does not react to  $\gamma$  rays. Perfect discrimination is vitally important for all delayed-neutron investigations because the number of  $\beta$ -disintegration events with subsequent  $\gamma$  decay is substantially greater than the number of  $\beta$ -decay events with subsequent neutron emission.

The best neutron-energy measurements available, those by Batchelor et al.,<sup>29</sup> give nearly continuous spectra for the various time groups, with the following centroids:

- 250 keV for group 1 (55 sec),
- 460 keV for group 2 (22 sec),
- 405 keV for group 3 ( 6 sec),
- 450 keV for group 4 ( 2 sec).

Groups 1 and 2 differ most with respect to energy (by a factor of 1.8). Here the  $^3\text{He}(n,p)^3\text{H}$  cross section differs by a factor of 1.4 because of its  $1/v$  relation. In the 10-mm-thick polyethylene moderator between source and  $^3\text{He}$  counter tubes, the neutrons are subject to an average of about six collisions. Energies on leaving the moderator plate are about 40 keV (group 1) or 70 keV (group 2). The  $^3\text{He}$  counter tubes are already "gray" for these energies, so there is a 20% difference in detection probability for groups 1 and 2. The counter tubes are "darker" for the neutrons scattered by lateral and rear moderator walls, so 20% is a high estimate. One should further note that the energetically lower half-life group 1 (essentially  $^{87}\text{Br}$ ) contributes only about 4% to the total yield, whereas the energetically equal half-life groups 2 through 4 constitute 81%. At least for saturated neutron-activity measurements, the  $^3\text{He}$  counter tubes can therefore be assumed to have approximately the same detection probability for all delayed neutrons, independent of energy.

Since each delayed neutron decay is initiated by a precursor  $\beta$  decay, the neutrons are emitted in coincidence with  $\beta$  particles. This fact can be used to improve the signal-to-background ratio by

operating a  $\beta$  detector of good configuration (in the present case a proportional counter tube with methane circulation) in coincidence with the  $^3\text{He}$  counter tubes. Figures 7 and 8 show the geometric layout of  $n$  and  $\beta$  detectors for buildup and damping measurement.

Before entering the sensitive volume of the  $\beta$ -proportional counter tube, the  $\beta$  particles pass through the following absorbers (see Fig. 7):

nylon transport band, thickness  $10 \text{ mg/cm}^2$ ;  $^2$  Hostaphan-vacuum window, thickness  $11 \text{ mg/cm}^2$ ; Hostaphan foil, vapor-coated with aluminum, used as  $^2$  counter-tube window, thickness  $1 \text{ mg/cm}^2$ .

From the energy-range relationship it follows that the detectable  $\beta$  energy has a 170-keV lower limit for the entire  $22\text{-mg/cm}^2$  surface density. The electronic threshold can be neglected by comparison.

The maximum energy available for  $\beta$  decay is the difference of the  $Q$  value,  $Q_\beta$ , for  $\beta$  decay of the parent nuclide and the neutron-binding energy,  $B_n$ , in the neutron emitter. For the known neutron emitters, the difference,  $Q_\beta - B_n$ , averages 2.8 MeV.<sup>42</sup> The maximum possible  $\beta$  energy is reduced by the 400-keV average neutron energy to 2.4 MeV. Assuming an allowed  $\beta$ -decay spectrum, the counting loss for this energy and the threshold mentioned would be 5%. Corresponding computations for the extreme ( $Q_\beta - B_n$ ) cases of 4.0 and 2.0 MeV yield counting losses of 1 and 12%, respectively. Accordingly, the detection probability of the  $\beta$ -proportional counter is assumed to have a maximum deviation of  $\pm 6\%$  from the average.

To determine the optimum coincidence resolution period, neutron time-of-flight spectra were produced for different arrangements of moderator and cadmium shield. During a number of test cycles, the neutron time-of-flight spectra were recorded in a 1024-channel TMC multichannel analyzer using the time-of-flight module. The pulse from the  $\beta$  counter started, and that from the neutron detector stopped, the time-of-flight measurement. This determination of coincidence resolution time takes into account both the electron collection time in the proportional counters and the neutron moderation time. Figure 10 is an example of a time-of-flight spectrum (resolution time  $0.25 \mu\text{sec}$ ). Zero time is shifted by including a fixed delay in the

neutron branch, so that even the ascending leg can be clearly examined. The time-of-flight measurements lead to the following optimum conditions for coincidence measurement:

thickness of the polyethylene moderator between source and  $^3\text{He}$  counters: 10 mm;  
cadmium shield directly around  $^3\text{He}$  counters;  
delay of the (faster)  $\beta$ -counter tube as compared to the  $^3\text{He}$  counter tubes:  $10 \mu\text{sec}$ ;  
coincidence resolution time:  $2\tau = 14.0 \mu\text{sec}$ .

The number of random coincidences is governed by the single rates  $R_\beta$  and  $R_n$  in both counters.  $R_\beta$  is determined by the time and mass relationship of the fission-product  $\beta$ -decay events.<sup>26</sup>  $R_n$  derives from the constant reactor-hall background (1 pulse per sec) and from two time- and mass-dependent rates--the neutron-emission rate from the irradiation section, and the emission rate from the testing section. In each instance, only one of the latter contributions leads to real coincidence events; all other contributions must be considered in the random-coincidence correction. The many  $\beta$  particles that do not lead to neutron emission, although they are emitted by fission products from the source, and the large coincidence resolution time require a correction for random coincidences.

Although the coincidence requirement reduces the counting rate by a factor of 2 to 5, this disadvantage is more than balanced by improvement in the signal-to-background ratio. The ratio of real to random coincidences reaches a maximum of about 100. Under favorable conditions the ratio is two orders of magnitude better than that without the coincidence requirement.

#### 3.4. Electronic Equipment and Control.

The electronic equipment shown in Fig. 11 was used for buildup and damping measurements. The pulse from the  $^3\text{He}$  counter tubes is transmitted directly to the coincidence stage, that from the  $\beta$  counter tubes with a  $10\text{-}\mu\text{sec}$  delay. The coincidence stage resolving time is approximately adjusted to the  $14\text{-}\mu\text{sec}$  optimum resolving time. Its exact value is determined from the random coincidence rate of two radioactive specimens. The coincidence signals are registered by the multiscaler module of a 1024-channel TMC multichannel analyzer.

At the beginning of a buildup measurement cycle, the central electronic clock opens the rapid

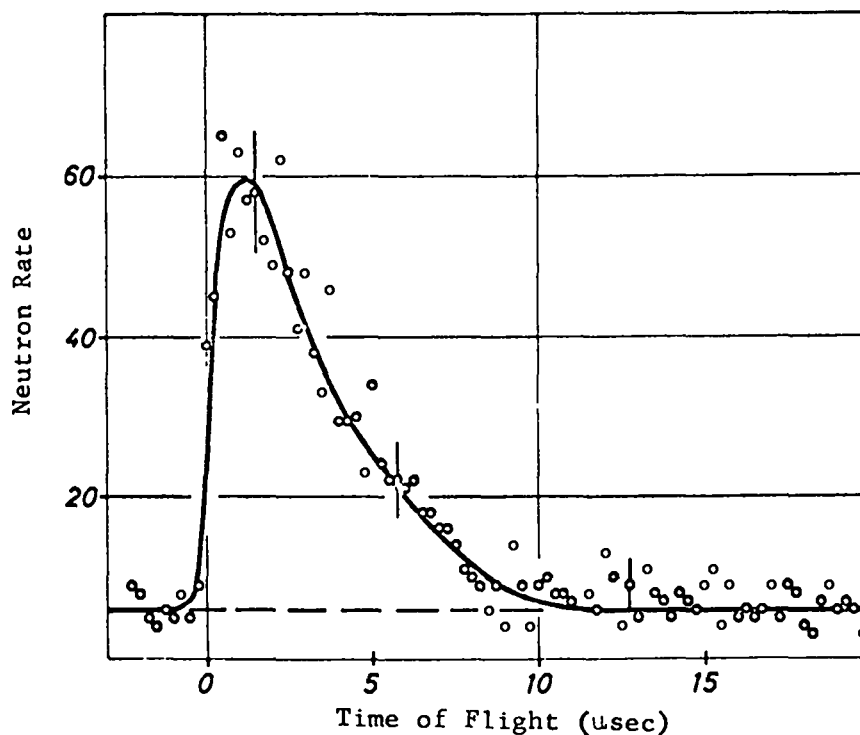


Fig. 10. Neutron time-of-flight spectrum.

shutter and simultaneously sets the zero point for time analysis in the multiscaler. After the time,  $T$ , desired for buildup has been reached, the clock stops the multiscaler, closes the rapid shutter, and gives an order to the transport device. During an irradiation cycle for damping measurement, the clock gives orders for transport (time 0) at the beginning (time  $t_1$ ) and on completion (time  $t_2$ ) of the multiscaler analysis.

These measurement cycles are repeated at a fixed magnetic field, and the data registered in the multiscaler are added until the rate statistics are satisfactory. After the appropriate number of cycles, the multichannel memory is automatically read out, and the magnetic field is set to a new value. By changing the magnetic field, one can cover the entire fission-product mass range. All single rates and coincidence rates are registered by scales and printed out at regular intervals. These rates serve for checking proper measurement performance, and the single  $\beta$  rate permits determination of the uranium foil burnup which cannot be neglected for the long measurement periods.

The time functions of the single rates  $R_p$  and  $R_n$  are recorded under identical conditions for each  $B\beta$  value for which a coincidence multiscaler spectrum was measured. The time-dependent rate,  $2\tau R_p R_n$ , of the random coincidence was computed from the single rates and the measured coincidence resolving time,  $2\tau$ , and subtracted from the coincidence rate. The number of cycles necessary for single-rate measurement is governed by the signal-to-background ratio and the error of the measured coincidence rate, and therefore differs for different time ranges and  $B\beta$  values.

#### 4. MEASUREMENT

##### 4.1. Buildup Measurement.

The apparatus shown in Fig. 7 was used to perform buildup measurements for 10 different  $B\beta$  values each for the light and heavy fission-product groups, in each case under optimum separator operating conditions. The neutron activity buildup was registered in a cycle until 100 sec after opening of the high-speed shutter. At this time all of the identified neutron emitters (see Sec. 5.2) are saturated except  $^{87}\text{Br}$ ,  $^{88}\text{Br}$ , and  $^{137}\text{I}$ , which have

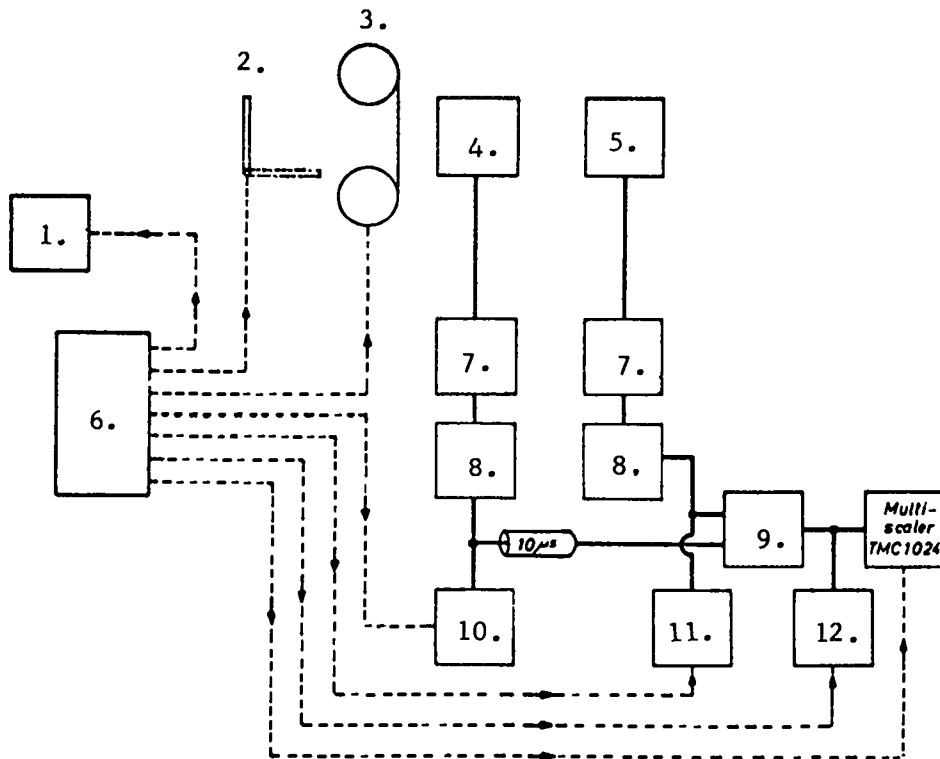


Fig. 11. Block diagram of electronic equipment.

- |                           |                                      |
|---------------------------|--------------------------------------|
| 1 - Magnet current supply | 7 - Preamplifier                     |
| 2 - Fast shutter          | 8 - Linear amplifier                 |
| 3 - Transport device      | 9 - Coincidence stage                |
| 4 - $\beta$ counter tube  | 10 - $R_{\beta}$ scaler              |
| 5 - n counter tube        | 11 - $R_n$ scaler                    |
| 6 - Central time control  | 12 - $R_{\text{coincidence}}$ scaler |

reached 71, 99, and 94% of saturation activity, respectively. This means that after 100 sec the known neutron emitters have reached 98% of their saturated activity.

Figure 12 is an example of a multiscaler spectrum after 300 buildup cycles in the mass 92 range. The coincidence events registered in the linearly consecutive multiscaler time channels were combined so that equidistant points were obtained in a logarithmic time scale. Furthermore, all counting rates for this example and for all damping curves shown below were standardized to a uniform counting time of  $10^3$  seconds. Total measuring time required to obtain the coincidence spectrum shown in Fig. 12 was 9.5 h. The random-coincidence time distribution of this BP value was computed from the measured single-rate buildup and subtracted from the measured effect.

Figure 13 presents all buildup curves measured for light fission products after random-coincidence correction, and Fig. 14 shows the corresponding heavy-fission product data. Because neither the  $\frac{1}{B}$  correction nor the radiation-intensity correction (which differs for light and heavy fission products) has been made, the light fission-product buildup curves (Fig. 13) cannot be compared with those for heavy fission products.

In Figs. 13 and 14 are shown the statistical errors that result from the measured coincidence rate and random-coincidence correction. Compared to these errors, detection-probability deviations for the neutron and  $\beta$  detectors are negligible (see Sec. 3.3). For long periods after the end of irradiation, particularly for the saturated activity at 100 sec, there are many superimposed single activities, so that the maximum deviations of de-

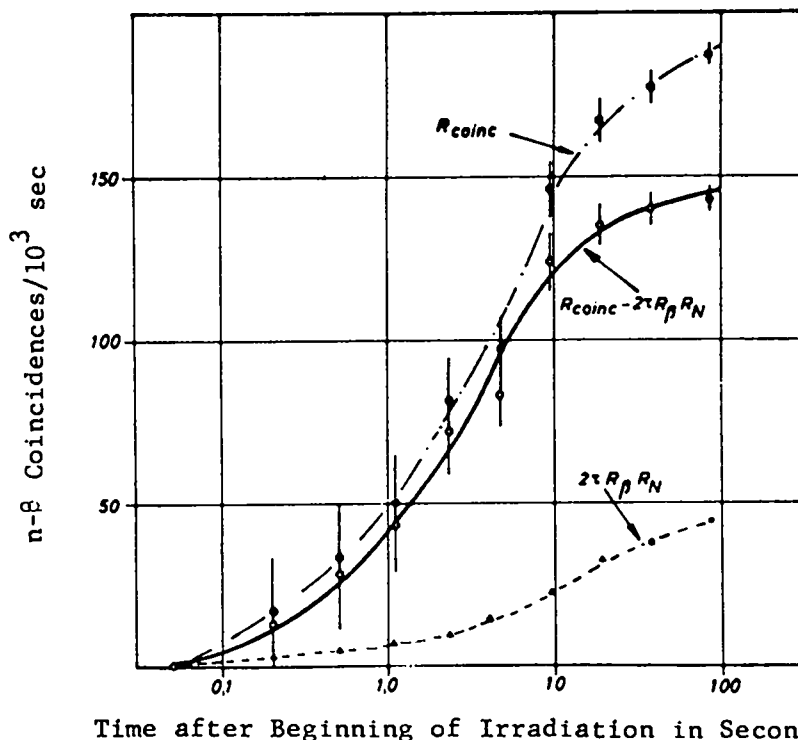


Fig. 12. Typical buildup curve.  $R_{\text{coinc}}$  = measured coincidence rate,  $2\tau R_{\beta} R_N$  = computed random-coincidence rate.

tection probability mentioned in Sec. 3.3 are substantially reduced.

#### 4.2. Damping Measurement.

The assembly shown in Fig. 8 was used to obtain damping curves at 18 Bp values for different irradiation periods. Cycle times for light fission products were 152, 52.8, 18.8, 3.42, and 1.23 sec, and those for heavy fission products were 44.8, 7.78, and 1.88 sec. Figure 15 shows, as an example, the damping curve in the mass 88 range after 1700 cycles of 18.8 sec each, as well as the correction for the computed random-coincidence rate. The counting interval per test point and cycle for the 18.8-sec cycle is 1 sec; accordingly, the total counting time per data point for 1700 cycles for the example shown in Fig. 15 is 1700 sec. For all damping curves shown below, the total counting time per data point has been normalized to  $10^3$  sec. For the 18.8-sec cycle this is equivalent to standardizing the number of cycles at 1000.

Figure 16 is a three-dimensional plot of all damping curves for light fission products as a function of Bp value. In addition to the Bp co-

ordinate, the figure also gives the average mass,  $\bar{A}$ , resulting from convolution of the radiochemical yield distribution with the apparatus resolution according to Eq. (A8). Standardization of the rates to a counting time of  $10^3$  sec per data point gives a standardized number of cycles for each cycle duration, which is shown at the ordinate in each case. The random-coincidence correction has been made. Net counting time for the damping curves shown in Fig. 16 was about 14 days. The uranium source burnup during this period cannot be neglected. For this reason, we checked the radiation intensity at regular intervals, both directly by means of a semiconductor counter, and through the  $\beta$  activity of the collecting foil (single  $\beta$  rate). All damping curves are corrected for burn-up.

Figure 17 shows the data from damping measurements for heavy fission products, processed in the same manner. The distributions shown in Figs. 16 and 17 are neither corrected for 1/B, nor adjusted to equal radiation intensity. Furthermore, the damping curves contain systematic errors be-

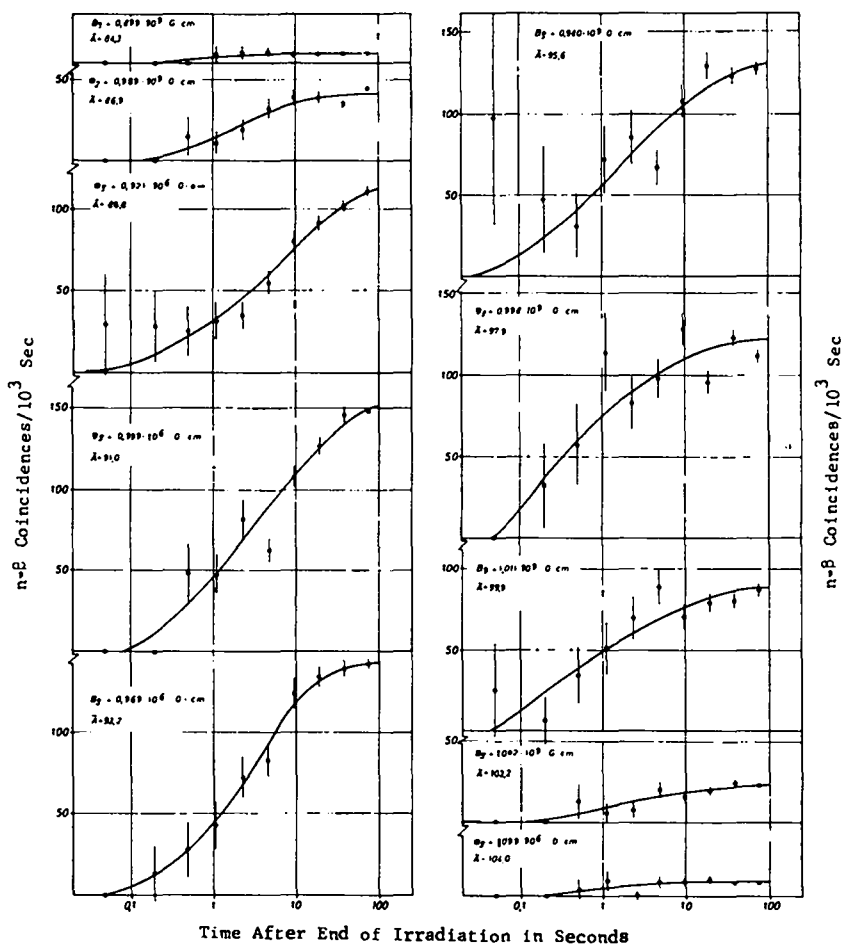


Fig. 13. Light fission-product activity buildup curves.

cause of the differences in detection probability for neutron and  $\beta$  detectors described in Sec. 3.3. These errors are discussed in Sec. 5.2.

## 5. RESULTS AND DISCUSSION

### 5.1. Measurement Evaluations.

The necessary corrections for burnup, depletion by recoil, and beam intensity were applied to the buildup curves recorded in Figs. 13 and 14; then the activities at 0.1, 1, 10, and 100 sec after the start of irradiation were subtracted for each  $B_0$  value. The results are summarized in Fig. 18. Investigation of heavy fission-product buildup until 0.1 sec after start of irradiation was omitted because of insufficient yield or excessive measurement error. The average mass,  $\bar{A}$ , is again given in addition to the magnetic field,  $B$ .

As stated in Sec. 3.1, with appropriate calibration, the activity value for time  $T$  after the start of irradiation is the number of neutrons emitted  $T$  seconds after fission. Because calibra-

tion is performed on the basis of the saturated activity reached 100 sec after the start of irradiation, this distribution is discussed first. It represents the mass distribution of the total yield. Figure 19 shows again the corrected 100-sec test values as a function of the magnetic field. Separate integration of the light and heavy mass ranges shows that  $67 \pm 3\%$  of all delayed neutrons are emitted by light fission products, and only  $33 \pm 3\%$  by heavy fission products. The entire mass-range integral is made to agree with the total yield of  $1.58 \pm 0.05$  delayed neutrons/100 fissions as given by Keepin<sup>37</sup> for thermal fission of  $^{235}\text{U}$ . Note that the neutron activities of the parent nuclides  $^{87}\text{Br}$ ,  $^{88}\text{Br}$ , and  $^{137}\text{I}$  are not completely saturated 100 sec after the start of irradiation. This means that on the basis of the neutron yields of these nuclides (see Sec. 5.2, Table III) the integral should be set equal to 1.55 neutrons/fission for calibration. This

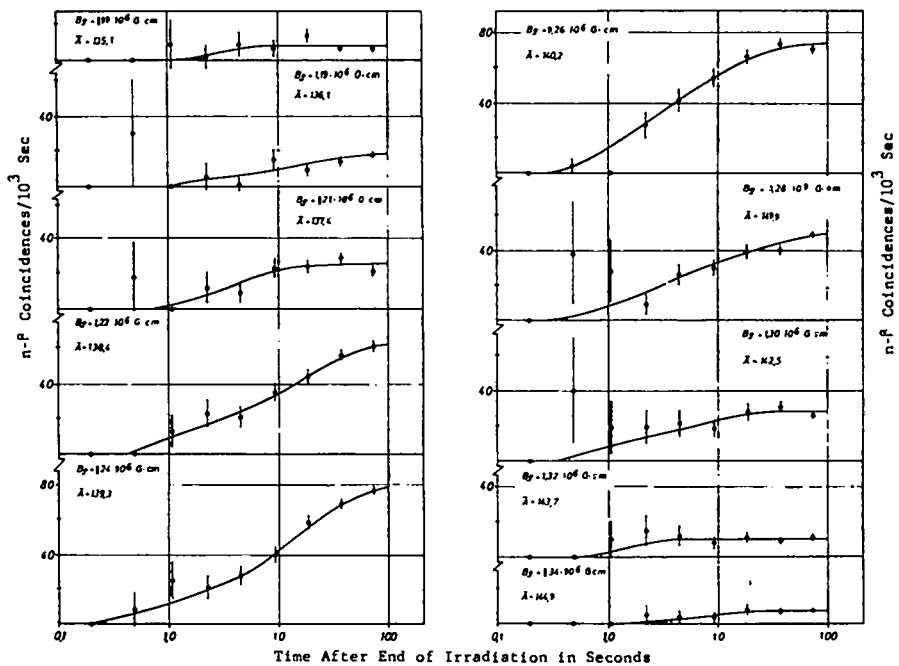


Fig. 14. Heavy fission-product activity buildup curves.

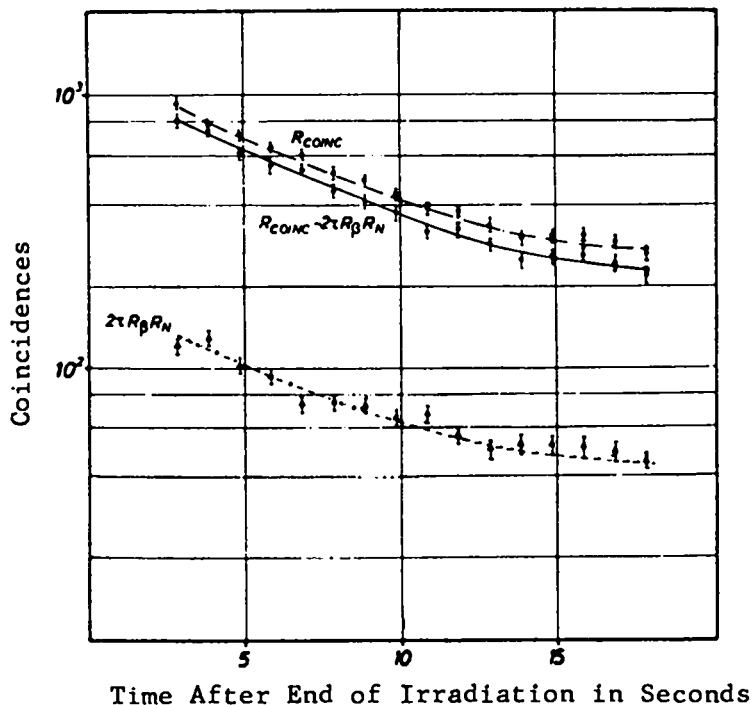


Fig. 15. Typical damping curve.  $R_{\text{coinc}}$  = measured coincidence rate,  $2\tau R_B R_N$  = computed random-coincidence rate.

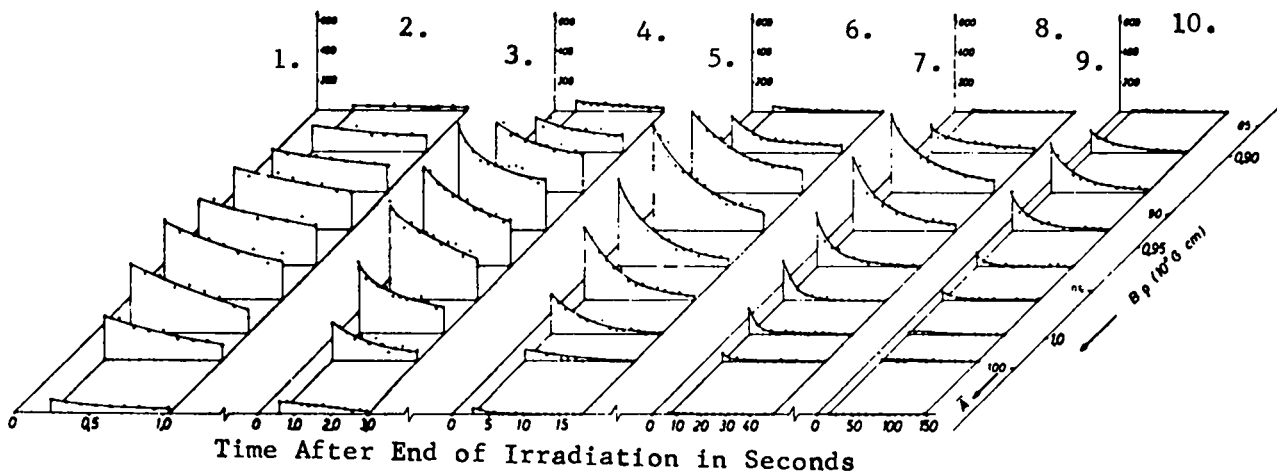


Fig. 16. Damping curves for different cycle durations as a function of mass (light fission products).

- |   |                                       |
|---|---------------------------------------|
| 1 - Coincidences/ 10,000 cycles = 0.1 sec | 6 - 1,000 exposures at 18.8 sec each. |
| 2 - 10,000 exposures at 1.23 sec each     | 7 - Coincidences/ 333 cycles = 3 sec  |
| 3 - Coincidences/ 5,000 cycles = 0.2 sec  | 8 - 333 exposures at 52.8 sec each    |
| 4 - 5,000 exposures at 3.42 sec each      | 9 - Coincidences/ 100 cycles = 10 sec |
| 5 - Coincidences/ 1,000 cycles = 1 sec    | 10 - 100 exposures at 15.2 sec each   |

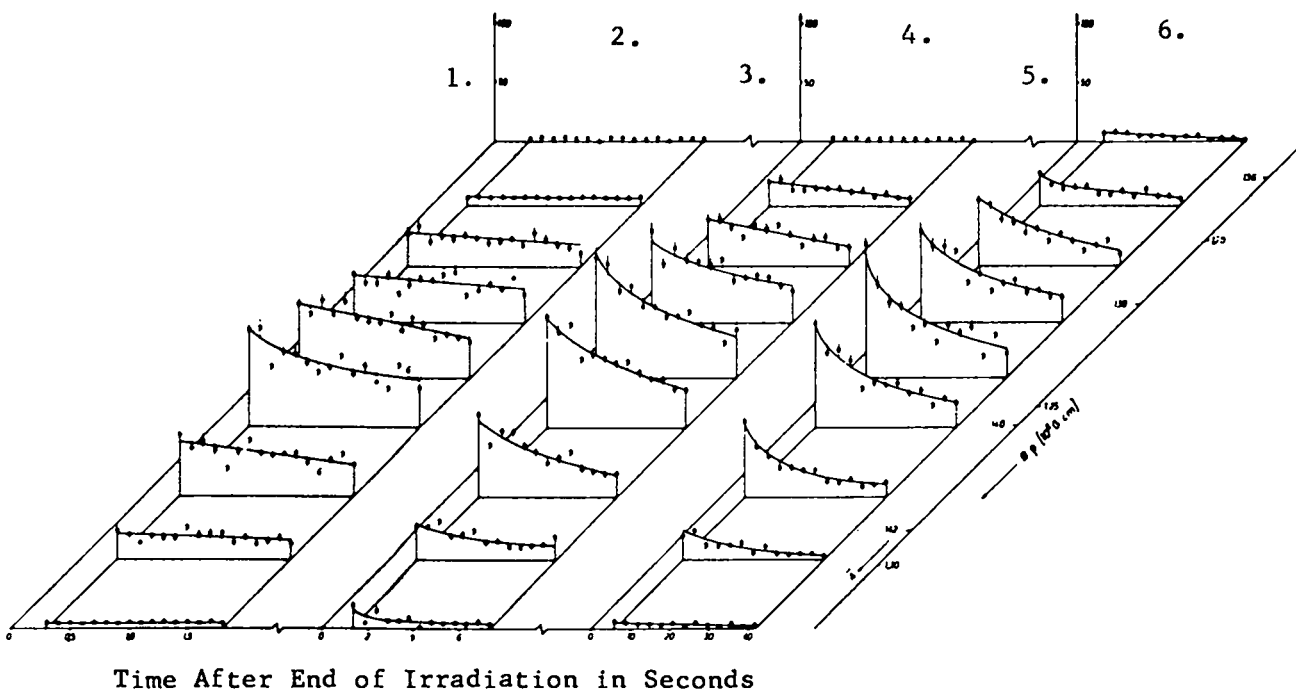


Fig. 17. Damping curves for different cycle durations as a function of mass (heavy fission products).

- |   |
|---|
| 1 - Coincidences/ 10,000 cycles = 0.1 sec |
| 2 - 10,000 exposures at 2.09 sec each     |
| 3 - Coincidences/ 2,000 cycles = 0.5 sec  |
| 4 - 2,000 exposures at 8.64 sec each      |
| 5 - Coincidences/ 333 cycles = 3 sec      |
| 6 - 333 exposures at 45.0 sec each        |

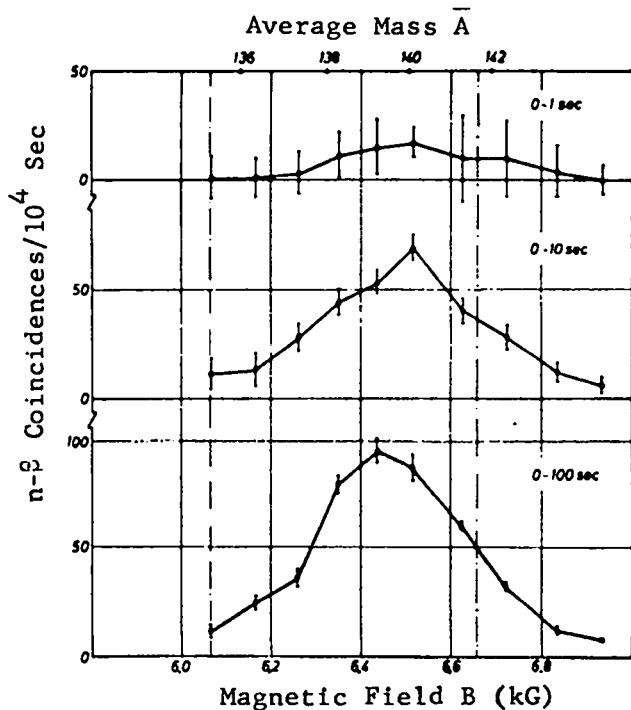
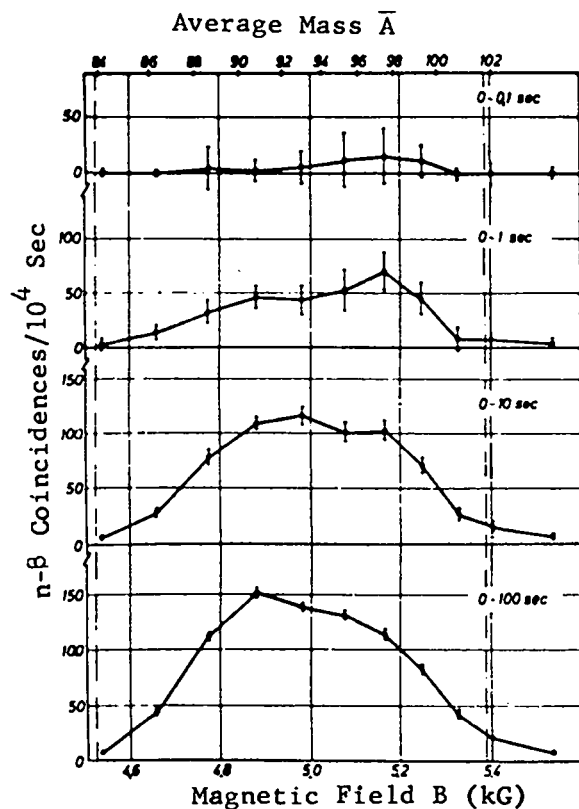


Fig. 18. Mass distribution of neutron activity 0.1, 1, 10, and 100 sec after start of irradiation.

yields absolute values of  $1.05 \pm 0.06$  and  $0.53 \pm 0.04$  neutrons/ 100 fissions of light and heavy fission products, respectively.

Integrating the distributions summarized in Fig. 18 in a similar manner gives the neutron yield at different times after fission and for corresponding time intervals, separately for light and heavy fission products. The results listed in Table I indicate, for instance, that most delayed neutrons are emitted from 1 to 10 sec after fission.

An obvious analysis of the damping curves shown in Figs. 16 and 17 would be to resolve the complex decay curve into its separate components. However, such analysis is not possible because of the large errors in the test points. Instead, the curves are characterized by the following variables:

1. Total intensity under the damping curve, integrated with respect to decay duration, and
2. Average half-life  $\overline{T_{1/2}}$ . This is determined by a least-squares-fit of the test data performed assuming only one half-life.

Figure 20 shows the resulting integrals of intensity for the different damping curves. The integral rates are standardized for a counting period of  $10^4$  sec. This condition means different "normalized" cycle numbers depending on cycle duration; in each instance the products of "normalized" cycle number and counting period for a cycle are shown along the ordinate. In addition, the irradiation time,  $T_B$ , and the representative average half-life,  $\overline{T_{1/2}}$ , are shown for each distribution.

The behavior of  $\overline{T_{1/2}}$  expressed as a function of the  $B_p$  value will be discussed in the next section. All distributions are corrected for burnup and recoil depletion, but the results for light and heavy fission products cannot yet be compared with respect to intensity.

In passing within the light fission-product group from a 152-sec cycle duration to shorter irradiation periods, the intensity distribution increases both in magnitude and width. Whereas neutron emission for an average 35-sec half-life occurs only in the 86 to 91 mass range, the yield distribution in the second range extends over practically the entire light mass range. Because of the inferior mass dispersion, only a small shift of the

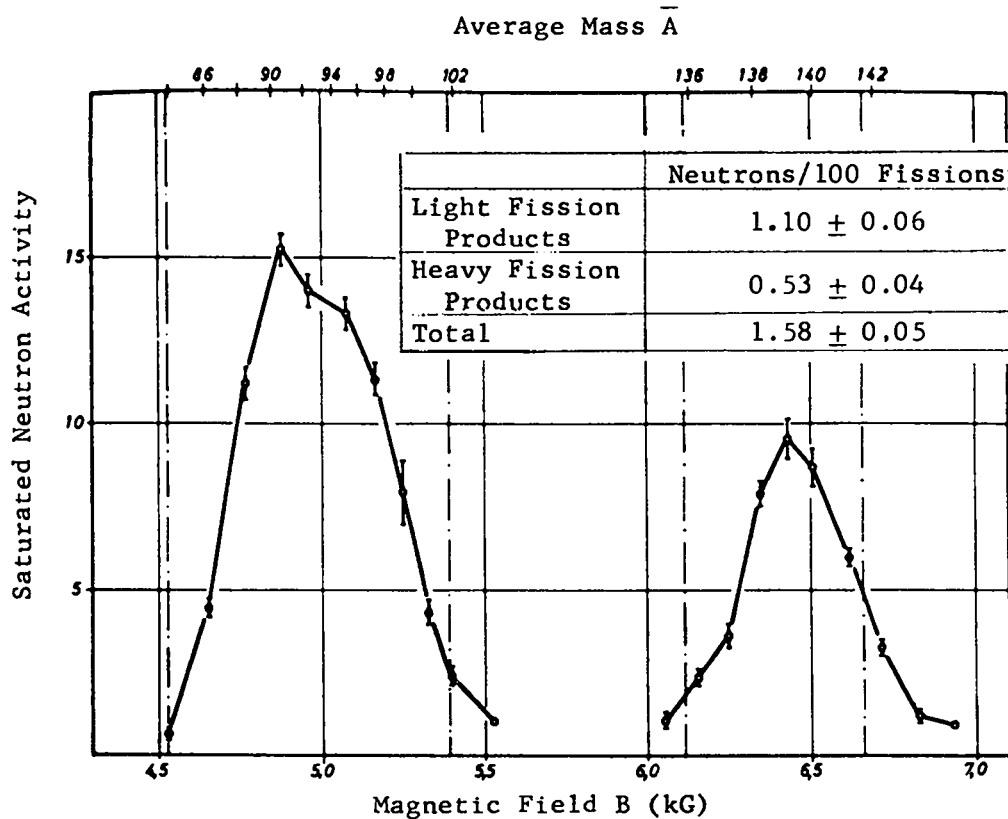


Fig. 19. Mass distribution of saturated neutron activity.

TABLE I  
NEUTRON YIELDS FOR DIFFERENT TIMES AND TIME INTERVALS AFTER FISSION

Neutron Yield (neutrons/100 fissions)

	Time after Fission (sec)				Time Interval (sec)		
	0.1	1	10	100	0.1-1	1-10	10-100
Light Fission Products	0.06 $\pm 0.06$	0.39 $\pm 0.11$	0.80 $\pm 0.07$	1.03 $\pm 0.06$	0.33 $\pm 0.13$	0.41 $\pm 0.13$	0.23 $\pm 0.09$
Heavy Fission Products		0.09 $\pm 0.04$	0.37 $\pm 0.04$	0.52 $\pm 0.04$		0.28 $\pm 0.05$	0.15 $\pm 0.06$

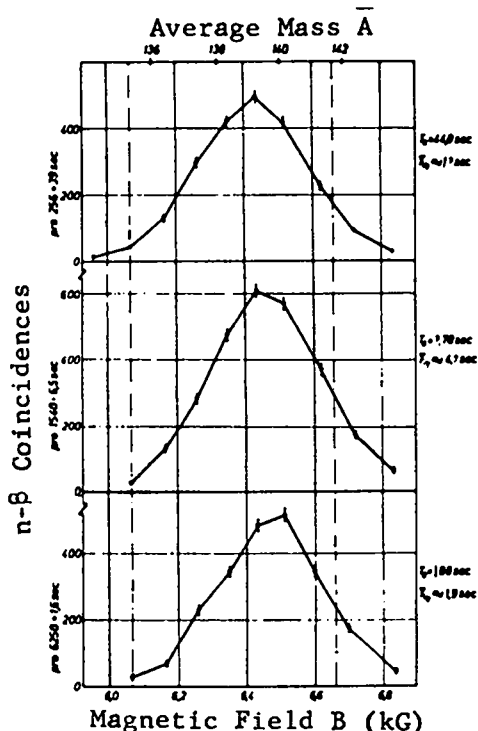
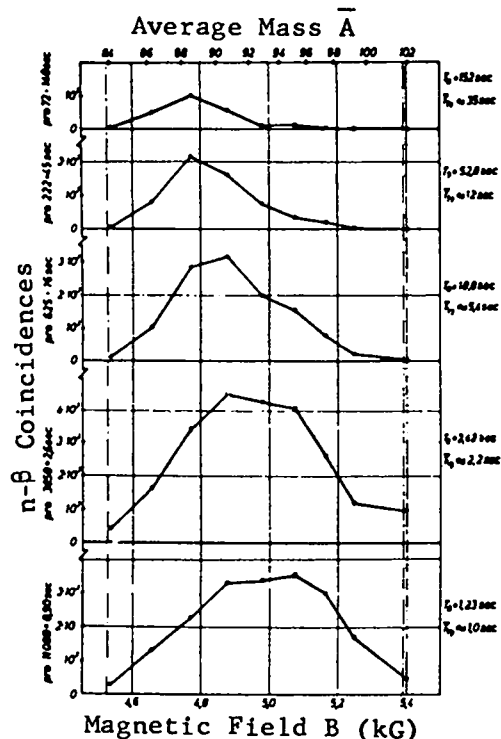


Fig. 20. Mass distribution of the damping-intensity integral for different cycle durations.

short heavy fission-product half-lives toward higher mass can be detected.

Table II lists the results obtained for different cycle durations by separate integration for the light and heavy mass range, respectively. For the time being, the integration gives only relative values because the coincidence counter assembly in the detector section of the transport system has not been calibrated. This calibration, performed using known neutron emitters and described in detail in the next section, gives the yields shown in the last line of Table II. At first glance, these yields appear very high, but one should recall that the time resolution of the discontinuous transport system is moderate, so that a very wide half-life range is covered in any cycle duration. Nevertheless, a clear maximum is apparent at 1 to 2 sec in the light fission-product half-life spectrum. This shape roughly resembles the yield distribution in the six-group analysis of gross neutron yield.<sup>3</sup>

#### 5.2. Comparison With Known Neutron Emitters.

Various authors have identified a number of nuclides as parents of delayed neutron emitters. These are summarized in Table III, as of early 1968, to the extent that yield determinations are available in addition to mere identification, and to the extent that identification can be considered reliable.

For <sup>85</sup>As, we accepted the mass correlation by Del Marmol et al.,<sup>6</sup> and the yield is the average of their results and Tomlinson's.<sup>7</sup>

For the parent nuclides <sup>87</sup>Br, <sup>88</sup>Br, and <sup>89</sup>Br, two methods are available for determination of  $P_{n,c} Y_c$ . The first is based on the branching ratios,  $P_n$ , as computed by Aaron et al.<sup>5</sup> and, together with the computed cumulative yields,  $Y_c$ , gives a set of  $P_{n,c} Y_c$  values. The computation of  $Y_c$  (see Table III, column 2) was based on the centers,  $Z_p$ , of primary nuclear charge distribution computed by Reisdorf,<sup>31</sup> which agree well with more recent tests performed with the Jülich mass separator.<sup>24</sup> Following a proposal by Wahl,<sup>32</sup> we assumed the shape of primary charge distribution in a mass chain to be a Gaussian curve with the breadth parameter  $c = 0.86$ . Because of discrepancies among the nuclear charge distributions given by different authors, a deviation of  $\pm 0.2$  charge units from Reisdorf's value was allowed for  $Z_p$ . This deviation leads to the

TABLE II  
NEUTRON YIELDS FOR DIFFERENT HALF-LIFE RANGES

Test No.	Light Fission Products					Heavy Fission Products		
	1	2	3	4	5	6	7	8
Irradiation Period $T_B$ (sec)	152	52.8	18.8	3.42	1.23	44.8	7.78	1.88
Average Half-Life $T_{1/2}$ (sec)	35	12	5.4	2.2	1.0	17	4.1	1.9
Yield, neutrons/100 fissions	0.11	0.30	0.55	0.92	0.84	0.21	0.26	0.25

errors given for  $Y_c$ .

The second set of  $P_n Y_c$  for  $^{87-89}\text{Br}$  is obtained from the relative yields determined for these parent nuclides by Perlow and Stehney<sup>4</sup> and Herrmann et al.<sup>9</sup> Following a proposal by Keepin,<sup>3</sup> the yield of  $^{87}\text{Br}$  is taken as equal to the absolute yield of 0.058 neutron/100 fissions for the 55-sec group as obtained from gross neutron activity analysis. This addition is suggested by tests by Williams et al.<sup>32</sup> which show that less than 0.5% of the 55-sec group are due to a parent nuclide other than  $^{87}\text{Br}$ . The last column of Table III shows the  $P_n Y_c$  averages for  $^{87-89}\text{Br}$  determined by the two methods.

The yield of  $^{90}\text{Br}$  can be obtained only from relative yield.  $P_n$  measurements by Amiel et al.,<sup>10</sup> Herrmann et al.,<sup>9</sup> and Amarel et al.<sup>12</sup> are available for  $^{93}\text{Kr}$  and  $^{90-96}\text{Rb}$ ; these, together with the computed cumulative yields, give the values of  $P_n Y_c$  shown.

The following were used in the heavy fission-product group: the iodine isotopes  $^{137}\text{I}$  and  $^{138}\text{I}$ , for which  $P_n Y_c$  could again be determined in two ways;  $^{139}\text{I}$ ; and  $^{140}\text{I}$ , which Herrmann et al.<sup>9</sup> recently identified as a parent nuclide. Agreement of relative iodine yields with the 0.220-neutron/100 fissions yield that Cox et al.<sup>33</sup> measured for the 20-sec group in spontaneous  $^{252}\text{Cf}$  fission is established. As in Ref. 33, we assume that the heavy fission-product neutron yields for  $^{252}\text{Cf}$  fission are the same as those for  $^{235}\text{U}$  fission, and that light fission products do not appreciably

contribute to the above group yield.

Del Marmol's evaluation<sup>34</sup> was used to determine the unambiguity of an identification. Accordingly, we did not include in Table III the parent nuclidea  $^{91}\text{Kr}$  and  $^{92}\text{Kr}$  reported by Day et al.<sup>11</sup> although they later reported<sup>35</sup> a conspicuously high 27%  $P_n$  yield for  $^{92}\text{Kr}$ , whereas Amiel et al.<sup>10</sup> could find no evidence of  $^{91}\text{Kr}$  and  $^{92}\text{Kr}$  neutron activity. The systematics of delayed neutron emission are another point against  $^{91}\text{Kr}$  and  $^{92}\text{Kr}$  being parent nuclides. Slight neutron activities for  $^{141}\text{Xe}$  and  $^{142}\text{Cs}$  observed by Day et al.<sup>11</sup> and Amarel et al.<sup>12</sup> were not considered either. Finally,  $^{134}\text{Sb}$ , recently identified by Tomlinson et al.,<sup>8</sup> and  $^{135}\text{Sb}$ , reported by Tomlinaon et al.<sup>7</sup> and Del Marmol et al.,<sup>6</sup> were not included in the set of identified parent nuclides because neutron-yield data are not available.

The neutron yields listed in Table III show errors of between 20 and 100%. The yields determined by different methods differ in some cases by a factor of 2 to 3 which far exceeds the reported errors. We could find no explanation for the discrepancy in different authors' data. The following computation is based on the yields listed in the last column of Table III; however, the absolute values must be systematically reduced as will be shown.

To compare the neutron activities measured by the mass separator using known neutron yields, the yields are convoluted with the resolving power of the apparatus on the basis of the mass-calibration

TABLE III  
IDENTIFIED PARENT NUCLIDES

Parent Nuclide	$P_n(\%)$	$Y_c(\%)$	$P_n Y_c (10^{-4})$	Relative Yield	Addition $P_n Y_c (10^{-4})$	$P_n Y_c (10^{-4})$	Assumed Value $P_n Y_c (10^{-4})$	Reference
$^{85}\text{As}$			$5.9 \pm 1.6$ $4.8 \pm 1.2$				$5.2 \pm 1.0$	6, 7
$^{87}\text{Br}$	$3.1 \pm 0.6$	$2.0 \pm 0.3$	$6.2 \pm 1.7$	$0.37 \pm 0.08$ 0.4	$5.8 \pm 0.7$	$5.8 \pm 1.4$	$6.0 \pm 1.1$	3, 4, 5, 9
$^{88}\text{Br}$	$6.0 \pm 1.6$	$2.0 \pm 0.5$	$12.0 \pm 4.4$	1.00		$15.7 \pm 3.8$	$14 \pm 3$	4, 5, 9
$^{89}\text{Br}$	$7 \pm 2$	$1.4 \pm 0.6$	$9.8 \pm 5.1$	$1.9 \pm 0.4$ 1.7		$28.2 \pm 7.1$	$16 \pm 4$	4, 5, 9
$^{90}\text{Br}$				$1.5 \pm 0.6$		$22.7 \pm 9.8$	$23 \pm 10$	4, 9
$^{93}\text{Kr}$	$3.9 \pm 0.6$	$0.4 \pm 0.4$	$1.6 \pm 1.4$				$1.6 \pm 1.4$	10
$^{93}\text{Rb}$	$1 \pm 0.5$ $2.6 \pm 0.4$ $1 \pm 0.5$	$1.7 \pm 0.3$	$3.7 \pm 0.9$	$6.3 \pm 1.9$			$6.3 \pm 1.9$	9, 10, 12
$^{94}\text{Rb}$	$10 \pm 5$ $5 \pm 2.5$	$7.5 \pm 2.8$	$2.0 \pm 0.8$	$15.0 \pm 8.2$			$15 \pm 8$	9, 12
$^{95}\text{Rb}$	$6 \pm 3$	$0.8 \pm 0.5$	$4.9 \pm 3.8$				$5 \pm 4$	12
$^{96}\text{Rb}$	$10 \pm 5$	$0.2 \pm 0.2$	$2 \pm 2$				$2 \pm 2$	12
$^{137}\text{I}$	$3.0 \pm 0.5$	$3.9 \pm 1.1$	$11.7 \pm 3.8$	1.00	$22.0 \pm 2.4$	$22.0 \pm 3.3$	$18 \pm 3$	3, 4, 5, 9
$^{138}\text{I}$	$1.9 \pm 0.5$	$2.5 \pm 0.9$	$4.8 \pm 2.1$	$0.47 \pm 0.05$ 0.5		$10.3 \pm 1.5$	$8.5 \pm 1.3$	4, 5, 9
$^{139}\text{I}$				$0.38 \pm 0.05$ 0.8		$13.2 \pm 4.6$	$13.2 \pm 4.6$	4, 9
$^{140}\text{I}$				0.5		$11 \pm .11$	$11 \pm 11$	9

curve. In so doing, one must usually consider time factors for the known parent nuclides which describe the effect of half-life on the contributions made by the particular activities. For convolution (explained for fission-product distribution in the Appendix) using the mass-calibration curve (Figs. 3 and 4 (s)), each of the known parent nuclides is assigned the Bp value that governs deflection in the separator. For this, one must first compute the apparent mass shift,  $\Delta A$ , of these nuclides according to Eq. (9). The primary charge distribution enters into the computation through the term  $\Delta Z$ ; here again Reisdorf's<sup>31</sup> and Wahl's<sup>32</sup> data were used

for primary charge distribution. The mass dispersion,  $\Gamma$ , is taken from (b) Figs. 3 and 4. The shift,  $\Delta A$ , in mass units, for instance, of the three strongest emitters in the light fission-product group, is 0.3 for  $^{89}\text{Br}$ , 0.6 for  $^{90}\text{Br}$ , and 1.1 for  $^{94}\text{Rb}$ . Because of the appreciably greater mass dispersion for heavy fission products, mass shifts for them are substantially greater: 3.3 for  $^{137}\text{I}$ , and 7.3 for  $^{139}\text{I}$ .

As mentioned in Sec. 3.1, convolution for the buildup method can be performed according to Eq.

(A7) by substituting  $P_n^{(1)} Y_c^{(1)} \cdot \int_0^T v_1(t) dt$  for the

term  $\eta_i$  in that equation. The yields listed in the last column of Table III are used for  $P_n^{(i)} Y_c^{(i)}$ . The time factor  $\int_0^T v_i(t) dt$  can be replaced by  $(1 - e^{-\lambda T})$  by assuming that the neutron-emitting nuclide (decay constant  $\lambda$ ) is exclusively of primary origin or that the decay constants of all parent nuclides are large compared to  $\lambda$ .

Figure 21 shows the measured "saturated" distribution together with the result of convolution. As in Fig. 19, the measured values are shown by open circles as a function of the magnetic field or of average mass. The computed distribution is shown by dashed lines, and the known errors result from squared superposition of the yield errors listed in Table III.

The requirement that the computed distribution not exceed the measured distribution leads to the fit at the highest point of the measured distribution. This fit to the set of known yields means a further calibration. To obtain agreement of the integrals with the allowable 1.58 neutrons/100 fissions (see Sec. 5.1), the yields that formed the basis of convolution must be reduced. We performed this reduction as follows: assuming that the yields listed in Table III were in correct relation to each other and that their relative distribution was unchanged, we reduced all absolute light fission-product yields by 16%, and all absolute heavy fission-product yields by 21%. With the existing errors, this is entirely possible.

Comparison of the two distributions shows that the difference between measured and identified heavy fission-product activities is not clearly outside the limit of error. The difference may therefore be explained by appropriate increase of the known yields; there is no compelling indication of unknown activity in the mass range of heavy fission products. By contrast, part of the light fission-product group in the 95 to 100 mass range remains unidentified despite the considerable uncertainty of known yields. Table IV lists the identified and unidentified parts of the light and heavy fission products. Of the 1.05 neutrons/100 fissions emitted by light fission products, 0.77 can be considered known, and  $0.28 \pm 0.10$  are not yet identified.

An earlier publication<sup>37</sup> on part of this

study reported a substantially larger unidentified portion. This portion has since been partially assigned through identification of the parent nuclides  $^{93}\text{Kr}$  and  $^{93-96}\text{Rb}$ .<sup>9,10,12</sup>

Figure 22 shows the activity buildup test values 0.1, 1, 10, and 100 sec after start of irradiation, together with the convolution of the known neutron yields for light and heavy fission products. The unidentified part of the 95 to 100 mass range is being built up mainly in the interval from 0.1 to 1 sec. In this interval are also indications of slight unidentified activity in the 85 to 88 mass range, but this activity no longer shows in the saturated distribution.

Figures 23 and 24 compare the intensity integral and average half-life from the various damping measurements, expressed as a function of the  $B_0$  value, with the corresponding variables for known emitters. In each case, the measured intensities from Fig. 20 are plotted together with the computed intensity distribution in the upper halves of these figures. Convolution is performed according to Eq. (A7), with the yields,  $\eta_i$ , replaced by terms of the form  $P_n^{(i)} Y_c^{(i)} h_i \left( T_{1/2}^{(i)} / T_B \right)$ . The time factor,  $h_i$ , takes into account how much a parent nuclide of half-life  $T_{1/2}^{(i)}$  contributes to the activity integral at cycle duration  $T_B$ . The value of  $h_i$  is computed from Eq. (15), and the half-lives,  $T_{1/2}^{(i)}$ , are taken from Ref. 35. The average half-lives,  $\overline{T_{1/2}}$ , are plotted in the lower halves of Figs. 23 and 24. The open circles indicate the result of a least-squares fit to the damping curves shown in Figs. 16 and 17. The half-lives shown by dashed lines are obtained when damping curves constructed for the identified neutron emitters are also described by the above least-squares fit.

Figure 23(a) shows the results for light fission products at 152-sec cycle duration. In the  $B_0$  range studied, the known parent nuclides used for comparison (in this case essentially 55.7-sec  $^{87}\text{Br}$  and 15.9-sec  $^{88}\text{Br}$ ) lead to average half-lives of between 42 and 23 sec. The measured half-lives agree well with these values. The computed intensity distribution for the 152-sec cycle was fitted at one point to the measured intensity distribution [see Fig. 23(a)], which amounts to absolute calibration of the counter by means of the  $^{87}\text{Br}$  and  $^{88}\text{Br}$  yields. This calibration is maintained for

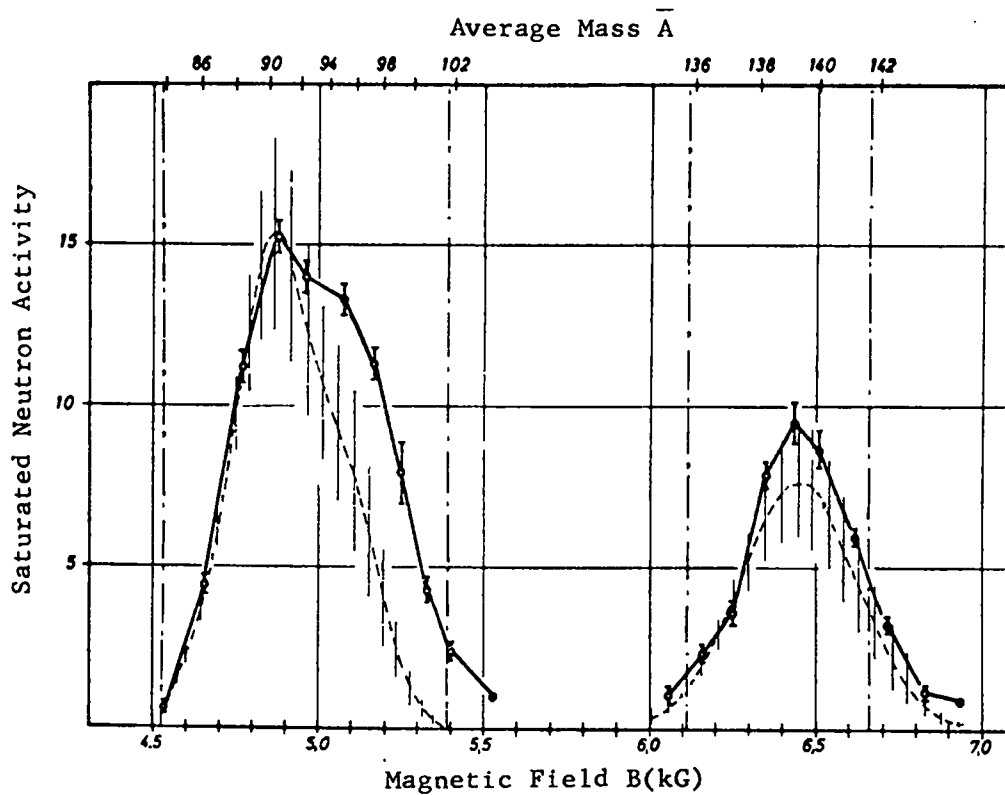


Fig. 21. Measured (o) and computed (---) mass distribution of saturated neutron yield.

TABLE IV  
IDENTIFIED AND UNIDENTIFIED PORTIONS OF NEUTRON YIELD

	Light Fission Products		Heavy Fission Products	
	Percent of Total Yield	Absolute, n/100 Fissions	Percent of Total Yield	Absolute, n/100 Fissions
Total Yield (1.58 ± 0.05 n/100 Fissions)	67 ± 3	1.05 ± 0.06	33 ± 3	0.53 ± 0.04
Identified Portion	51 ± 10	0.79 ± 0.15	25 ± 6	0.40 ± 0.10
Unidentified Portion	16 ± 7	0.26 ± 0.10	8 ± 7	0.12 ± 0.11

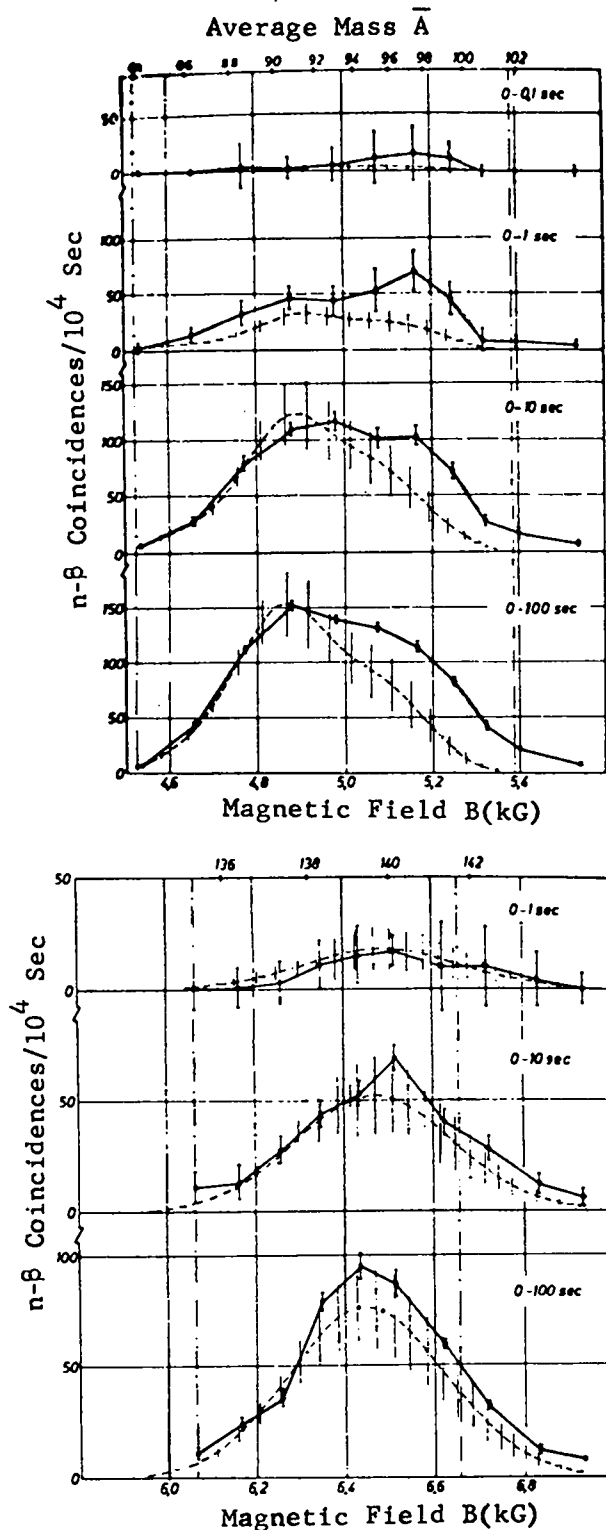


Fig. 22. Measured (o) and computed (---) mass distribution of neutron activity 0.1, 1, 10, and 100 sec after start of irradiation.

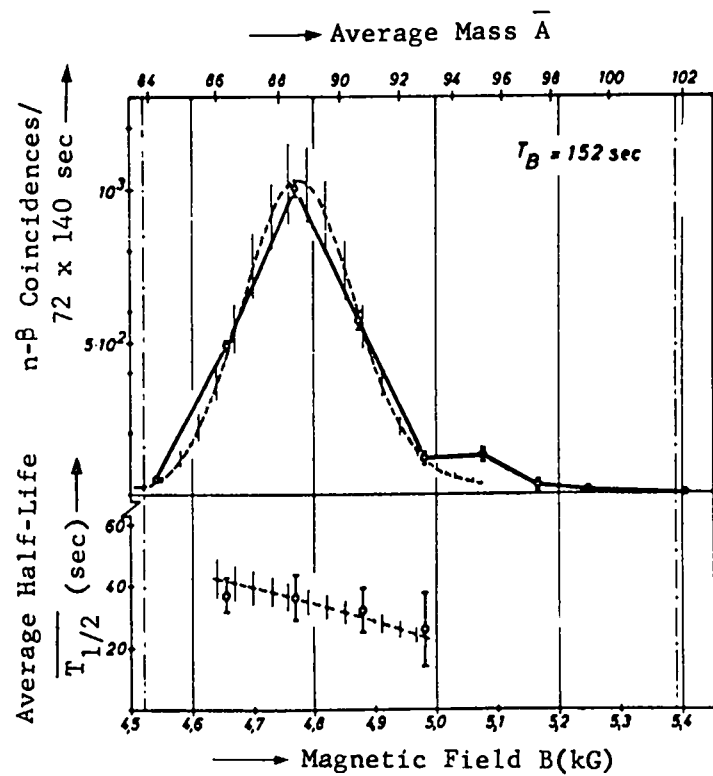
all light fission-product damping measurements.

The nonconstant detection probabilities of the neutron- and  $\beta$  detectors was not considered in the buildup method. However, this effect cannot be neglected in the damping measurements because only a few neutron emitters are contributing in each case. In the 152-sec cycle for which the intensity calibration is performed, the parent nuclides  $^{87}\text{Br}$  and  $^{88}\text{Br}$  are present in a mixture of about 1:1. Both parent nuclides show a difference,  $(Q_{\beta} - B_n)$ , which averages about 2.8 MeV for all known parent nuclides.<sup>42</sup> From this aspect the calibration is representative and not affected by the  $\beta$ -detector threshold.

Further, the effect of neutron energy on neutron-detector detection probability must be examined. The neutron energy of the parent nuclide,  $^{87}\text{Br}$ , which is responsible for half-life group 1, is smaller than the average neutron energy of the remaining groups. According to the estimates made in Sec. 3.3, the detection probability for the existing mixture of  $^{87}\text{Br}$  and  $^{88}\text{Br}$  is therefore about 10% above the average. However, this effect is not subsequently considered because it may lead to even greater increase of the unidentified portion of activity.

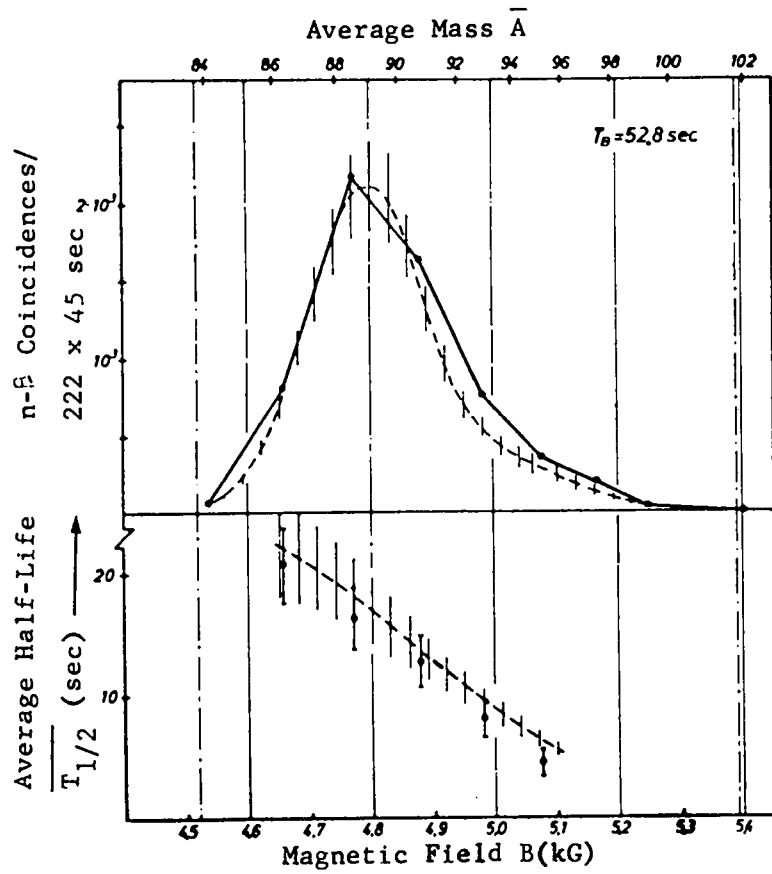
The good agreement between measured and computed intensity distribution in Fig. 23(a) also remains for cycle durations of 52.8 sec [Fig. 23(b)] and 18.8 sec [Fig. 23(c)]. Also, the average half-lives agree within the limits of error both as absolute values and as a function of  $B_p$ . This shows that for light fission products with  $T_{1/2} > 5$  sec there is no further unknown neutron activity of significant yield.

The measured intensity for cycle durations of 3.42 sec [Fig. 23(d)] and 1.37 sec [Fig. 23(e)] is higher than that computed. Therefore, the difference between measured and already identified intensity (i.e., the unidentified portion) of these two damping measurements was plotted in the middle sections of Figs. 23(d) and (e). The unidentified part of both measurements is primarily in the 95 to 100 mass range, with a smaller part in the 85 to 88 mass range. The appearance of unknown activity in the 95 to 100 mass range agrees with the buildup measurement results (see Fig. 21), which also indicated unidentified activity in the 85 to 88 mass

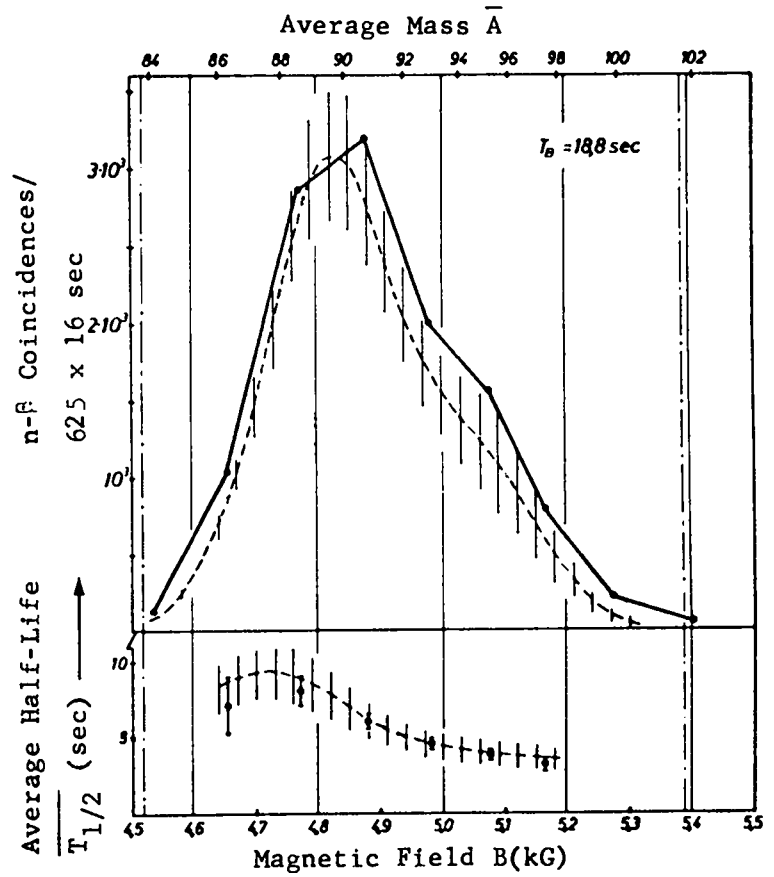


(a) 152-sec cycle duration

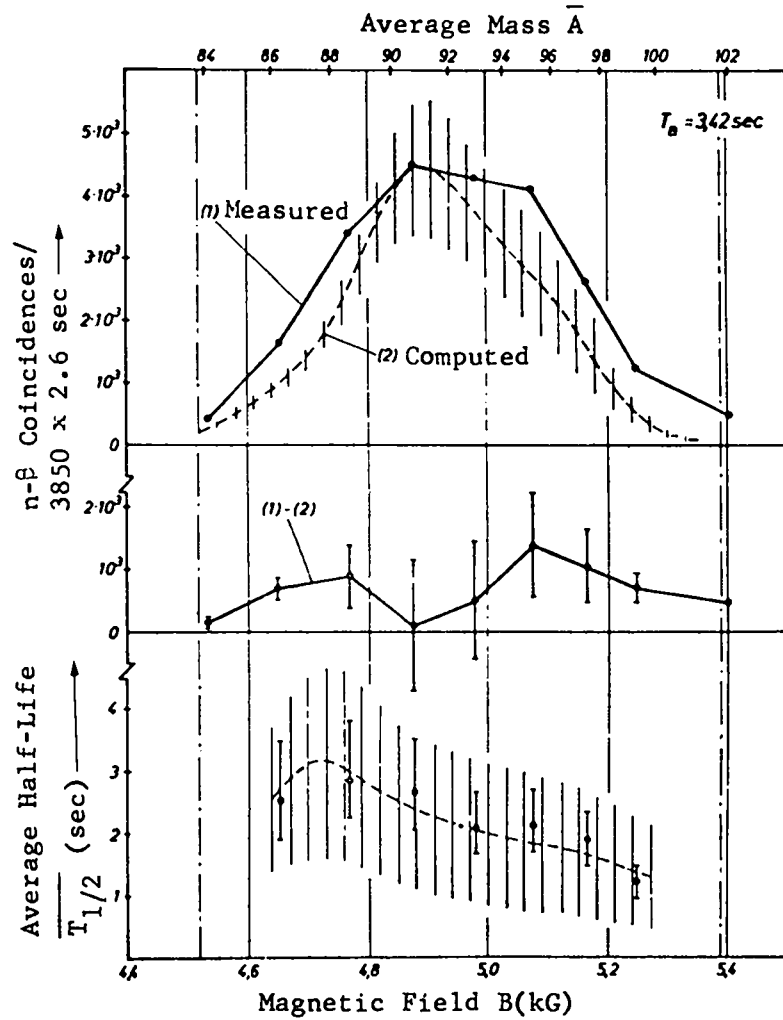
Fig. 23. Measured (o) and computed (---) mass distribution of light fission-product intensity and half-life.



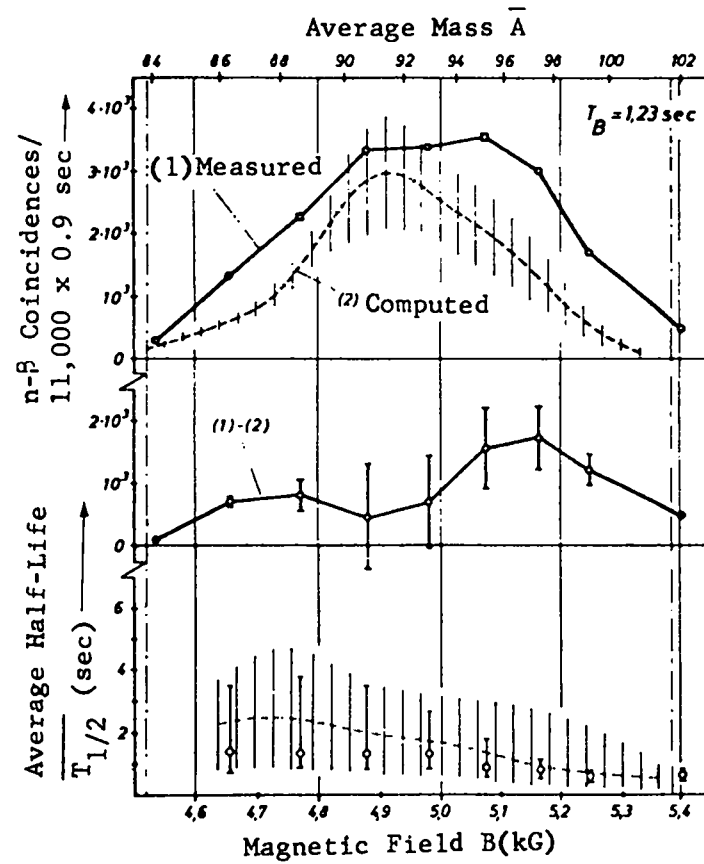
(b) 52.8-sec cycle duration



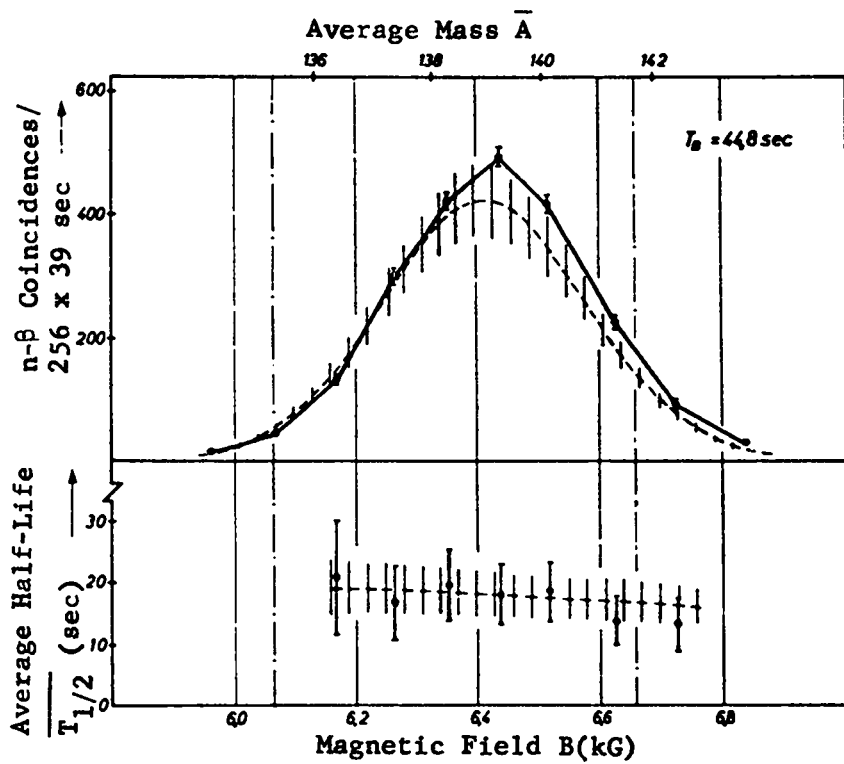
(c) 18.8-sec cycle duration



(d) 3.42-sec cycle duration

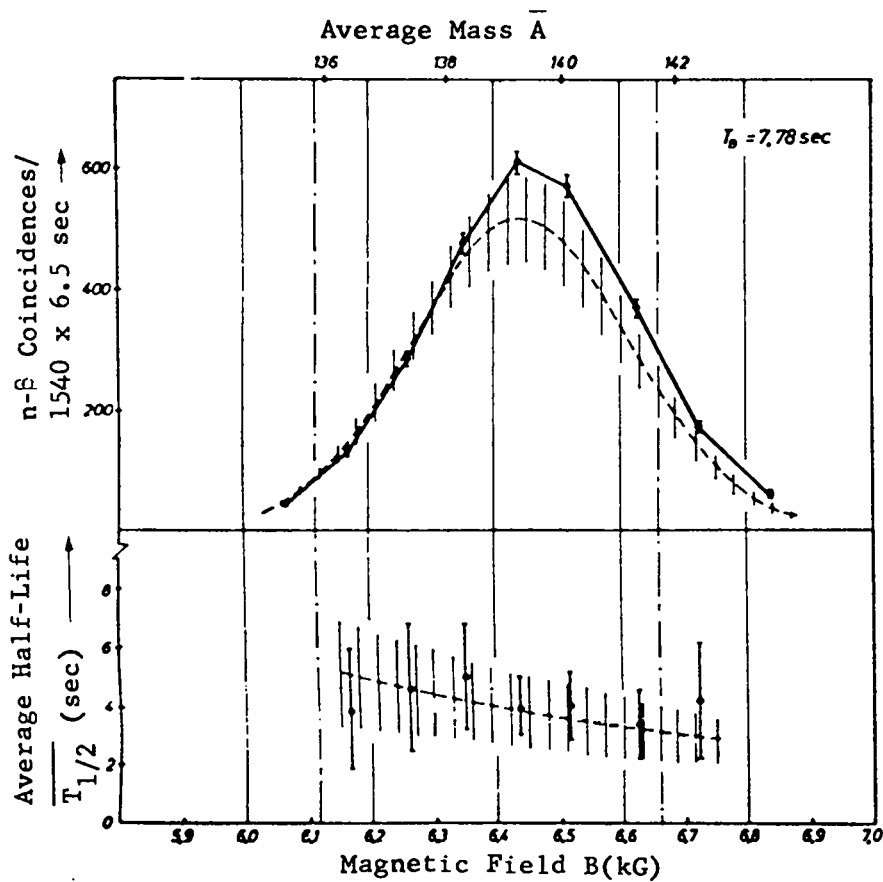


(e) 1.23-sec cycle duration

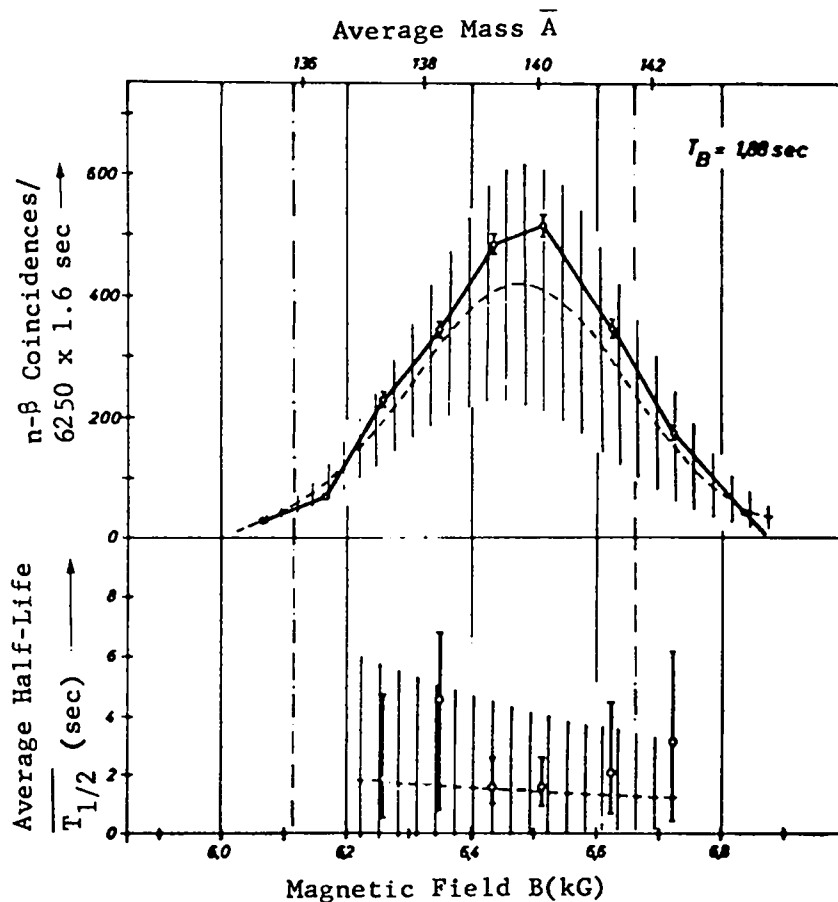


(a) 44.8-sec cycle duration

Fig. 24. Measured (o) and computed (---) mass distribution of heavy fission-product intensity and half-life.



(b) 7.78-sec cycle duration



(c) 1.88-sec cycle duration

range (see Fig. 22).

Basically, the average half-life of the unidentified part can be determined by comparing measured and computed half-life distribution; for this purpose, the mixing ratio of identified and unidentified activity can be found from the intensity curves. However, statements about half-life become more difficult for short cycle durations because the counting time in these cases is smaller than  $\overline{T_{1/2}}$ . As a result, the error in  $\overline{T_{1/2}}$  becomes large, and the unreliability especially increases toward long half-lives [unsymmetrical error band, see Fig. 23(e)]. The upper limit of  $\overline{T_{1/2}}$  is sometimes better defined by a longer cycle duration, and has therefore been adopted.

In the half-life distribution for the 1.23-sec cycle, Fig. 23(e), in the 85 to 88 mass range, the measured value (1.3 sec) is smaller than that computed (2.4 sec). Based on a 1:1 ratio between measured and computed intensity, this leads to an

unidentified activity half-life of about  $(0.2 \pm 0.2)^5$  sec. A corresponding calculation for the 3.42-sec cycle, Fig. 23(d), gives  $(2 \pm 2)^5$  sec, and the average for both measurements is  $(1 \pm 1)^5$  sec. The absolute yield of this activity is found to be  $P_{n,c} \approx 0.08$  neutron/100 fissions.

An obvious explanation for the unknown activity in the 85 to 88 mass range lies in increased neutron yield of the identified parent nuclide, 2.1-sec  $^{85}\text{As}$ . From the intensity curves, Figs. 23(d) and (e), one would expect a  $P_{n,c}$  value of 0.10 neutron/100 fissions for this nuclide. This is in contradiction to measurements by Del Marmol et al.<sup>6</sup> and Tomlinson<sup>7</sup> (see Table III). From Reisdorf's<sup>31</sup> and Wahl's<sup>32</sup> primary yield distribution,  $^{86}\text{As}$  and  $^{86-88}\text{Se}$  are therefore to be accounted for as still unidentified parent nuclides. The following half-life measurements are available for these nuclides: 16 sec for  $^{86}\text{Se}$  or  $^{87}\text{Se}$  according to Sattizahn et al.,<sup>38</sup> < 8 sec for  $^{87}\text{Se}$  according

to Norea et al.,<sup>39</sup> and 6 sec for <sup>87</sup>Se according to Tomlinson.<sup>40</sup> These data do not permit unambiguous limitation of the number of the nuclides mentioned. It is, furthermore, possible that at least part of the unknown activity can be attributed to a greater yield of 4.5-sec <sup>89</sup>Br than that shown in Table III,

The half-life of the unidentified activity in the 96 to 100 mass range is found to be  $(0.7 \pm 1.0)$  sec for the 1.37-sec cycle, and  $(2.7 \pm 1.9)$  sec for the 3.42-sec cycle, or an average of  $(1.5 \pm 1.8)$  sec. The absolute yield of this activity is  $P_{nc} Y_c \approx 0.20$  neutron/100 fissions, which agrees with buildup measurement.

On the basis of half-life and mass range, the known parent nuclides <sup>94-96</sup>Kr are a possible explanation. The neutron yields measured by various authors (see Table III) and general yield considerations preclude explanation by means of these known parent nuclides. With respect to primary yield, half-life, and mass (the latter under consideration of "Z-shift"), the nuclides <sup>97</sup>Sr, <sup>97-99</sup>Y, and <sup>99-100</sup>Zr can be considered parent nuclides of as yet unknown neutron emitters.

Eidens<sup>21</sup> has reported the following measurements and estimates of half-lives:  $\approx 0.4$ -sec <sup>97</sup>Sr, 1.1-sec <sup>97</sup>Y,  $\approx 0.8$ -sec <sup>99</sup>Y, 2.4-sec <sup>99</sup>Zr, and  $\approx 1$ -sec <sup>100</sup>Zr. All these values are consistent with the measured 1.5-sec half-life within the limits of error.

Figure 24 shows the intensity integral and average half-life for damping measurements with 44.8-, 7.78-, and 1.88-sec cycle durations performed with heavy fission products. The computed intensity distribution for the longest cycle duration is fitted to the left leg of the measured distribution. The measured intensity exceeds that computed for all cycle durations, but the difference is not clearly outside the limit of error. This state of affairs confirms that found in buildup measurement. The measured and computed half-lives agree well; as for light fission products, the half-life decreases toward higher masses. For the 7.78- and 1.88-sec cycles the measured values seem to deviate toward longer half-lives. This means that either the yields of the known iodine parent nuclides must be shifted toward long half-lives, or that the missing part is a relatively long-lived nuclide not considered in Table III,

e.g. 11-sec <sup>134</sup>Sb.<sup>8</sup> Further statements about heavy fission products are not possible because of the large dispersion in this mass range.

### 5.3. Systematics of Delayed Neutron Emission.

The measurements and comparison with known neutron emitters show the following possible new parent nuclides:

$${}^{86}\text{As} \text{ and } {}^{86-88}\text{Se}$$

$$T_{1/2} = (1 \pm 5) \text{ sec, } P_{nc} Y_c \approx 0.08 \text{ neutron/}$$

$$100 \text{ fissions}$$

$${}^{97-98}\text{Sr, } {}^{97-99}\text{Y, and } {}^{99-100}\text{Zr}$$

$$T_{1/2} = (1.5 \pm 1.8) \text{ sec,}$$

$$P_{nc} Y_c \approx 0.20 \text{ neutron/100 fissions.}$$

This allocation was made according to mass position and half-life of the unknown activity and considering the yield distribution. We will now examine whether the systematics of delayed neutron emission permit a selection among the above nuclides.

Pappas et al.<sup>41, 42</sup> and Keepin<sup>3, 43</sup> first attempted to compute neutron yields. The systematics applied herein are a modification of a recent study by Tomlinson.<sup>40</sup>

With increasing distance from the stable mass trough, the neutron binding energy decreases along an isobaric line, whereas the mass difference of neighboring nuclei, and thus the  $\beta$ -decay Q value, increase. The delayed-neutron emission threshold is the "contour" for which the Q value,  $Q_\beta(Z, N)$ , of the parent nuclide  $\beta$  decay equals the neutron binding energy,  $B_n(Z + 1, N - 1)$ , of the emitter.  $Q_\beta$  and  $B_n$  for nuclides far from the stable mass trough are generally not measured; only in a few cases can one obtain  $Q_\beta$  and  $B_n$  from measurements<sup>31, 44</sup> or by semiempirical extrapolation according to Way and Wood.<sup>44</sup> Wing and Fong's<sup>45</sup> mass formula was employed in all other cases. The  $Q_\beta$  and  $B_n$  computed by this formula are available in the form of tables.<sup>46</sup> The difference between computed and measured mass differences in the mass range examined averages  $\pm 0.5$  MeV for a distance of three charge units from the mass trough.

The resulting delayed neutron emission threshold is shown in Fig. 25 and 26 for light and heavy fission products, respectively. Because of the effect of pairing energy on  $Q_\beta$  and  $B_n$ , the neutron-emission threshold differs for parent nuclides with even and odd Z. The threshold of parent nuclides

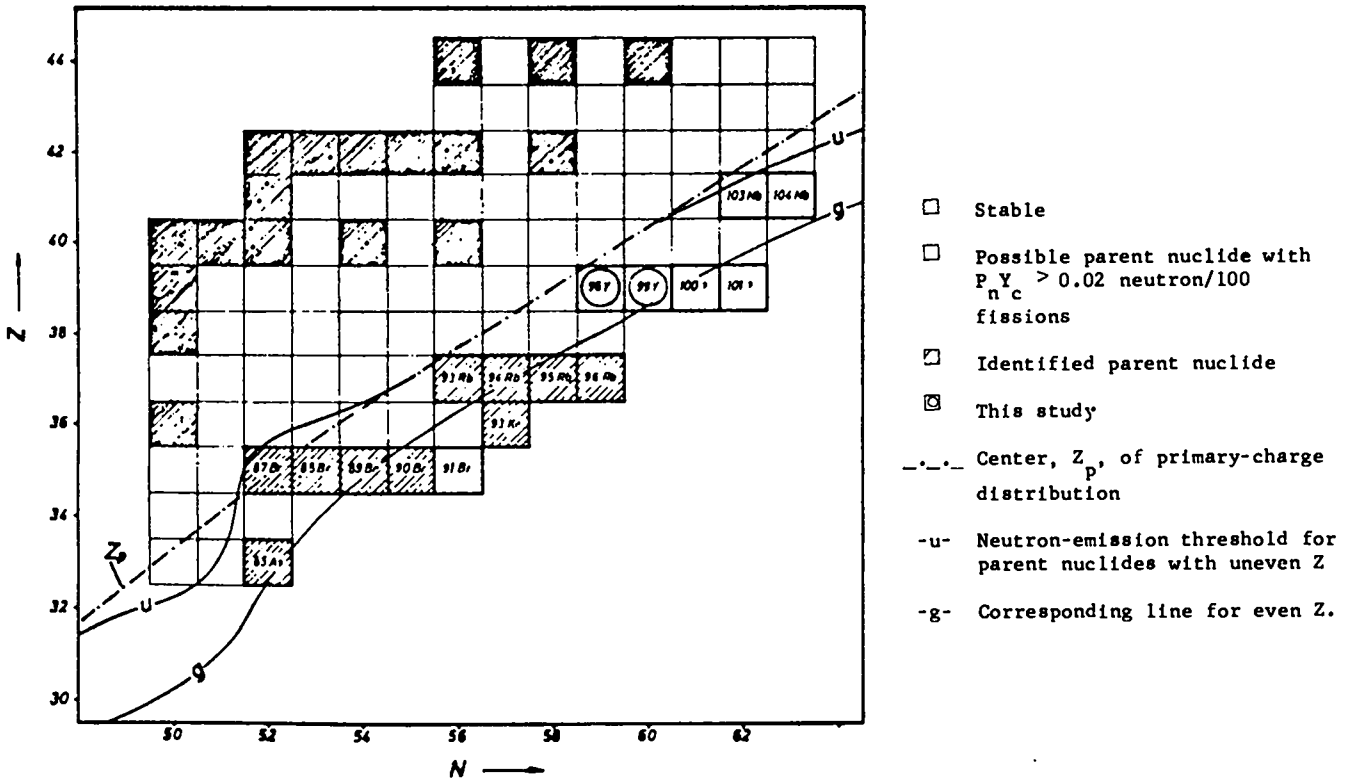


Fig. 25. Section of nuclide chart in the light fission-product mass range.

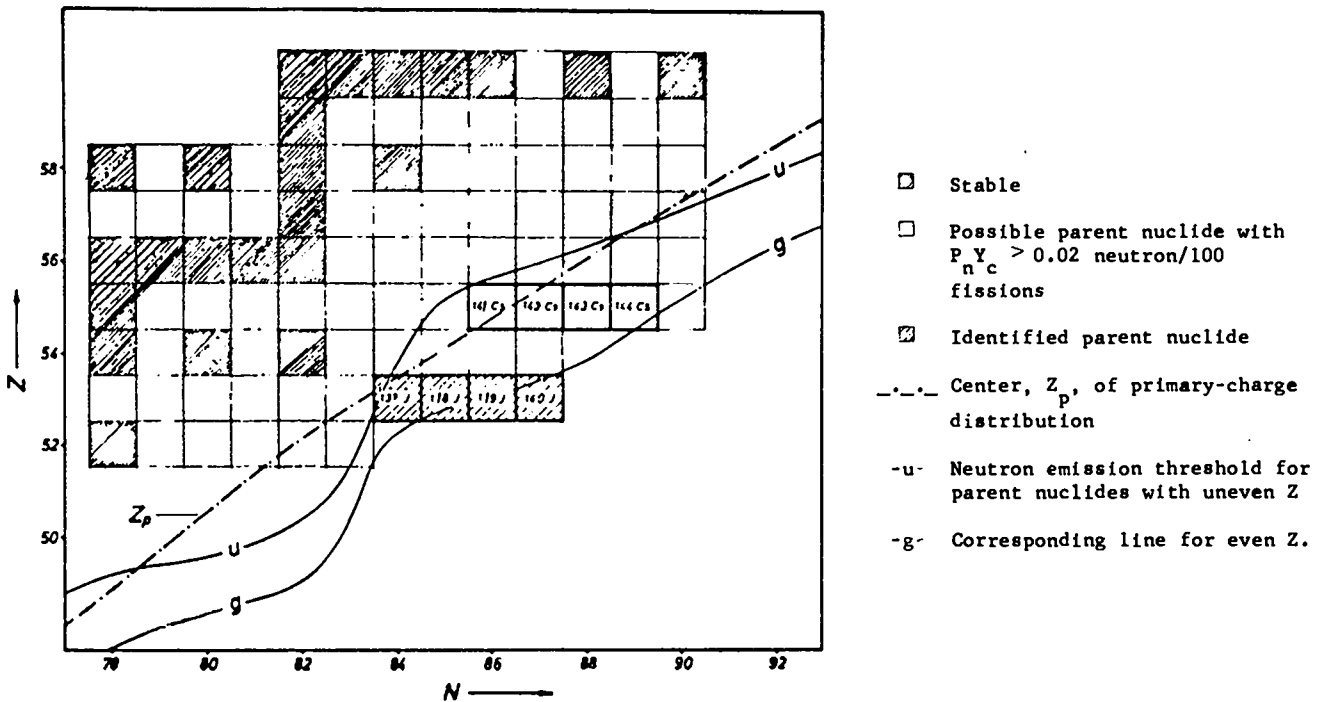


Fig. 26. Section of nuclide chart in the heavy fission-product mass range.

with odd  $Z$  is about two charge units closer to the stable mass trough for all masses than that of parent nuclides with even  $Z$ .

Neutron emission is possible with respect to energy only when the parent nuclide is located on the "uphill side" of the threshold. Because of this energy criterion,  $^{99}\text{Zr}$  and  $^{100}\text{Zr}$  are clearly eliminated from among the parent nuclides that might be considered on the basis of measurement.

The absolute yield,  $P_n Y_c$ , will be determined for parent nuclides for which neutron emission is energetically possible.  $Y_c$  is computed according to Reisdorf<sup>31</sup> and Wahl<sup>32</sup> as done earlier in Sec. 5.2. The center,  $Z_p$ , of primary nuclear-charge distribution<sup>31</sup> is plotted in Figs. 25 and 26. The branching ratio,  $P_n$ , between neutron- and  $\beta$ -decay events depends essentially on the spin and parity of the participating levels and on the distance,  $(Q_\beta - B_n)$ , from threshold.

In addition to the energy criterion, the absolute value of  $P_n Y_c$  is used as a second selection criterion. For clarity, only "strong" neutron emitters will be considered, i.e., yields  $> 0.02$  neutron/100 fissions. Because of the large discrepancy among various theoretical values of  $P_n$ ,<sup>41, 43</sup> the semiempirical  $P_n$ -value increase with distance from the threshold given by Tomlinson is adapted for  $P_n Y_c$  computation.

The following nuclides are located "on the threshold" and show an average difference,  $Q_\beta - B_n$ , of  $\pm 0.5$  MeV:  $^{84}\text{As}$ ,  $^{87}\text{Se}$ ,  $^{92}\text{Kr}$ ,  $^{92}\text{Rb}$ ,  $^{97}\text{Sr}$ ,  $^{97}\text{Y}$ ,  $^{103}\text{Zr}$ ,  $^{102}\text{Nb}$  and  $^{134}\text{Sb}$ ,  $^{136}\text{Te}$ ,  $^{134}\text{Xe}$ ,  $^{140}\text{Cs}$ , and  $^{147}\text{La}$ . None of these were considered "strong" parent nuclides, even in the few cases where the computed  $P_n Y_c$  barely exceeds 0.02 neutron/100 fissions. The justification for this assumption is that the available 0.5-MeV energy is inadequate to make the  $\beta$  decay sufficiently "fast." Of the nuclides mentioned,  $^{92}\text{Rb}$  could be excluded as a parent nuclide by experiment,<sup>12</sup> and  $^{140}\text{Cs}$  is out of the question because of its half-life.

In contrast to the nuclides mentioned,  $^{87}\text{Br}$  and  $^{137}\text{I}$  have  $(Q_\beta - B_n)$  values of 2.5 and 1.7 MeV, respectively, and are therefore already on the "uphill side" of the threshold. Accordingly, heavy contributions from these nuclides are already possible.

The effect of spin and parity on delayed neu-

tron emission has so far been discussed only in special cases; for instance, Pappas et al.<sup>42</sup> computed  $P_n$  values for the parent nuclides  $^{85}\text{As}$ ,  $^{87}\text{Br}$ , and  $^{135}\text{I}$  which agree well with the measured values. However, the necessary data for nuclei that are far from  $\beta$  stability are generally not sufficiently known. Accordingly, it might, indeed, be shown by the aid of spin and parity for initial and final  $\beta$ -n-decay conditions of the parent nuclides  $^{97}\text{Sr}$  and  $^{97}\text{Y}$ , which are of special interest here, that  $s$  neutrons can be emitted only after a forbidden  $\beta$  decay. However, since  $p$  neutrons already contribute at an energy of 50 keV above the threshold,<sup>42</sup> and because  $p$  neutron emission is possible in these cases after permitted  $\beta$ -decay events, a limitation of the  $P_n$  values is not possible on the basis of this consideration.

The resulting "possible and strong" parent nuclides for light and heavy fission products are plotted in Figs. 25 and 26, respectively. For light fission products, all 10 known parent nuclides (see Table III) also appear from systematics as "strong possible" parent nuclides. This fact justifies the at first somewhat arbitrary choice of the lower limit for  $P_n Y_c$ . In addition to the identified parent nuclides, systematics yield further possible parent nuclidea. By comparing these nuclides with the mass range possible on the basis of the measurements, we attribute the 1.5-sec activity in the 96 to 100 mass range ( $P_n Y_c = 0.20$  neutron/100 fissions) that has not been identified so far to the parent nuclides  $^{98}\text{Y}$  and  $^{99}\text{Y}$ . However, for the activity in the 85 to 88 mass range, we cannot clarify unambiguously whether  $^{86}\text{As}$  and  $^{87}\text{Se}$  provide small contributions in addition to the known parent nuclides  $^{85}\text{As}$  and  $^{89}\text{Br}$ . Furthermore, in agreement with the list of known parent nuclides given in Table III, systematics yield  $^{93}\text{Kr}$  as the sole parent nuclide with even atomic number. In the heavy fission-product case, only  $^{137-140}\text{I}$  and  $^{141-144}\text{Cs}$  are possible as strong parent nuclides according to systematics. All possible parent nuclides are identified (see Table III). Slight neutron activity has been reported for  $^{142}\text{Cs}$  and  $^{143}\text{Cs}$ ; for  $^{141}\text{Cs}$  and  $^{144}\text{Cs}$  no activity could be proven.<sup>12</sup>

The experimental finding that light fission products emit about twice as many delayed neutrons as do heavy fission products is qualitatively cor-

rectly represented by systematics. By simply counting the possible strong parent nuclides in the two mass ranges as a measure of neutron yield, one obtains 17 light and 8 heavy nuclides. The difference in neutron yields has the following causes (see Figs. 25 and 26): the widening of the mass trough with increasing mass number causes the neutron-decay threshold of heavy fission products to be about one charge unit further away from  $\beta$  stability than that of light fission products. On the outside, the  $Z_p$  distribution in both mass ranges is about equally far from  $\beta$  stability.<sup>24,31</sup> Although the difference in the threshold positions is partially compensated by the effect of neutron shells 50 and 82, this effect moves the odd-Z threshold of heavy fission products into the vicinity of the  $Z_p$  distribution in only a small range. For light fission products, however, the odd-Z threshold and  $Z_p$  distribution agree throughout the entire yield range.

The difference is accentuated because the increase in  $P_n$  with distance from the threshold was assumed to be about twice as strong for light as for heavy fission products, as in Ref. 40. We cannot check this assumption adequately with the few measured  $P_n$  values, but the overall balance would not change appreciably even if the  $P_n$  trend were the same for both mass ranges. The governing effects for delayed neutron emission systematics are the threshold position and the position and shape of the  $Z_p$  distribution.

Our systematics for delayed neutron emission provide qualitatively similar results to those prepared by Tomlinson, although he assumed a somewhat different  $Z_p$  distribution. The conclusions from these systematics contradict Keepin's prediction that parent nuclides among light fission products occur only up to <sup>97</sup>Rb. This observation<sup>43</sup> is based on both a different mass formula and a different  $Z_p$  distribution.

Strong neutron emission by the  $\Gamma$ -parent nuclides further contradicts a result obtained by Cowan et al.<sup>47</sup> which was confirmed by Herrmann et al.<sup>9</sup> Cowan et al. conclude from diffusion measurements that a large portion, possibly 80% or more, of the delayed neutron activity comes from bromine and iodine parent nuclides. Our measurements show, however, that only  $65 \pm 8\%$  of total yield is at-

tributable to bromine and iodine parent nuclides.

## 6. POSSIBILITIES FOR IMPROVEMENT OF THE METHOD

Construction of a new mass separator that will have better resolution and higher intensity than the apparatus described here is planned. Because of its better resolution, the new separator would permit more exact mass correlation, particularly of heavy fission products, and better statistics for damping curves would allow breakdown into several half-life components.

The transport device and electronic equipment might be improved as follows: an endless transport band could be used in the intermittently operating transport device to eliminate the rewinding which must be done every 30 min for 1-sec cycles using the existing 500-m-long band. Simultaneous registration of the various rates by a suitable multi-channel analyzer would be better than consecutive recording of time spectra per coincidence rates and single rates in the multiscaler.

The most important improvement would consist of measuring delayed-neutron energy. The energy spectra for gross neutron activity have so far been recorded with only moderate resolution,<sup>28-30</sup> and spectra for single neutron emitters have not been measured at all. Apart from general interest in energy spectra, energy measurement using a mass separator has the advantage that a third parameter, in addition to mass and half-life, becomes available for differentiation of neutron emitters. The method would then be equivalent to that used for identification of short-lived nuclides on the basis of their  $\gamma$  lines.<sup>20</sup> An energy resolving power of 10% would be sufficient for differentiation if each neutron emitter were characterized by a well-defined neutron energy, and if these energies for various emitters differed by about 10%. Such resolution capacity might be achieved with a neutron-time-of-flight spectrometer<sup>37, 48</sup> triggered by the  $\beta$  particle that precedes neutron emission, as in the time-of-flight measurement described in Sec. 3.3.

## SUMMARY

Delayed neutron emission in <sup>235</sup>U thermal neutron fission was investigated with a helium-filled mass separator. Neutron activity was measured in coincidence with the neutron emission that precedes  $\beta$  decay. Neutron yields at different times after

fission were obtained by measurement of activity buildup, and half-life distribution was obtained by measurement of activity damping.

The mass distribution of these variables was determined for the entire yield range. Total light fission-product neutron yield is 1.05 neutrons/100 fissions, but that of heavy fission products is only 0.53 neutrons/100 fissions. Measured mass dependence and time dependence are compared with published yields of identified neutron emitters. Unidentified portions of activity in the 85 to 88 (half-life 1 sec) and 96 to 100 (half-life 1.5 sec) mass ranges are discussed. The yield difference of light and heavy fission products is explained using delayed neutron emission systematics, and the so-far unidentified activity is attributed to the parent nuclides  $^{98}\text{Y}$  and  $^{99}\text{Y}$ .

#### ACKNOWLEDGMENTS

I am indebted to Dr. P. Armbruster, Director of the Department of Solid-State Physics and Neutron Physics of the Nuclear Research Center, Jülich, for his suggestion of the topic and for his constant support of the work through valuable discussion.

I am indebted to graduate physicist J. Eidens for cooperation in the construction of the separator and assistance in the experiment, to Dr. F. Hossfeld for providing the various computer programs, and to Messrs. J. W. Grueter, T. Kuenster, H. Lawin, and K. Sistemich for assistance in the measurements.

#### REFERENCES

1. R. Roberts, R. C. Meyer, and P. Wang, *Phys. Rev.*, 55, 510 (1939).
2. Panel on Delayed Fission Neutrons, Proc. IAEA, Vienna (1967).
3. G. R. Keepin, *Physics of Nuclear Kinetics*, Addison-Wesley, Part 4 (1965).
4. G. J. Perlow and A. F. Stehney, *Phys. Rev.*, 113, 1269 (1959).
5. P. M. Aron, O. I. Kostochkin, K. A. Petrzhak, and V. I. Shpakov, *At. Energ. (USSR)*, 16, 368 (1964).
6. P. Del Marmol and M. Neve de Mevergnies, *J. Inorg. Nucl. Chem.*, 29, 273 (1967).
7. L. Tomlinson, *J. Inorg. Nucl. Chem.*, 28, 287 (1966).
8. L. Tomlinson and M. H. Hurdus, *Phys. Letters*, 25B, 545 (1967).
9. G. Herrmann, Panel on Delayed Fission Neutrons, Proc. IAEA, Vienna (1967), p. 147, and private communication.
10. S. Amiel, J. Gilat, A. Notes, and E. Yellin, Panel on Delayed Fission Neutrons, Proc. IAEA, Vienna (1967), p. 115.
11. G. M. Day, A. B. Tucker, and W. L. Talbert, Panel on Delayed Fission Neutrons, Proc. IAEA, Vienna (1967), p. 103.
12. I. Amarel, R. Bernas, R. Foucher, J. Jastrzebski, A. Johnson, J. Teillac, and H. Gauvin, *Phys. Letters*, 24B, 402 (1967).
13. B. L. Cohen and C. B. Fulmer, *Nucl. Phys.*, 6, 547 (1958).
14. H. H. Heckman, E. L. Hubbard, and W. G. Simon, *Phys. Rev.*, 129, 1240 (1963).
15. H. D. Betz, G. Hortig, E. Leischner, C. Schmelzer, B. Stadler, and J. Weihrauch, *Phys. Letters*, 22, 643 (1966).
16. N. Bohr, *Mat. Fys. Medd. Dan. Vid. Selsk.*, 18, No. 8 (1948).
17. J. W. Grueter, Master's Thesis, College of Technology, Aachen (1968).
18. P. Armbruster, *Nukleonik*, 3, 188 (1961).
19. P. Armbruster, J. Eidens, and E. Roeckl, Proc. Intern. Symp. Why and How We Should Investigate Nuclides Far Off the Stability Line, Lysekil, Sweden, Aug. 1966, *Arkiv for Fysik*, 36, 293 (1967).
20. E. Hovestadt and P. Armbruster, *Nukleonik*, 9, 338 (1967).
21. J. Eidens, Ph.D. Thesis, College of Technology, Aachen (1968).
22. H. Farrar, H. R. Fickel, and R. H. Tomlinson, *Can. J. Phys.*, 40, 1017 (1962).
23. H. Farrar and R. H. Tomlinson, *Nucl. Phys.*, 34, 367 (1962).
24. P. Armbruster, Unpublished.
25. G. Alzmann, *Nukleonik*, 3, 295 (1961).
26. P. Armbruster and H. Meister, *Z. Physik*, 170, 274 (1962).
27. D. Hovestadt, Ph.D. Thesis, College of Technology, Munich (1963).
28. D. J. Hughes, J. Dabbs, A. Cahn, and D. Hall, *Phys. Rev.*, 73, 111 (1948).
29. R. Batchelor and H. R. McK. Hyder, *J. Nucl. Energy*, 3, 7 (1956).
30. T. W. Bonner, S. J. Bame, Jr., and J. E. Evans, *Phys. Rev.*, 101, 1514 (1956).
31. W. Reisdorf, *Z. Physik*, 209, 77 (1968).
32. A. C. Wahl, in "Physics and Chemistry of Fission," Proc. Salzburg Symp., IAEA, Vienna, Vol. I, p. 317 (1965).
33. E. T. Williams and C. D. Coryell, *Nucl. Appl.*, 2, 256 (1966).
34. S. Cox, P. Fields, A. Friedman, R. Sjoblom, and A. Smith, *Phys. Rev.*, 112, 960 (1958).
35. P. Del Marmol, "Summary of Experimental Data . . . . . Based on Reports to this Panel." Panel on Delayed Fission Neutrons. Proc. IAEA, Vienna (1967).
36. A. B. Tucker and G. M. Day, *Bull. Am. Phys.*

Soc., 12, 1179 (1967).

37. E. Roeckl, J. Eidens, and P. Armbruster, Panel on Delayed Fission Neutrons, Proc. IAEA, Vienna (1967), p. 85.
38. J. E. Sattizahn, J. D. Knight, and M. Kahn, J. Inorg. Nucl. Chem., 12, 206 (1960).
39. A. Notea and E. Yellin, Res. Lab. Annual Report IA-1082 (1965), p. 168.
40. L. Tomlinson, Panel on Delayed Fission Neutrons, Proc. IAEA, Vienna (1967), p. 61.
41. A. C. Pappas and G. Rudstam, Nucl. Phys., 21, 353 (1960).
42. T. Jahnsen, A. C. Pappas, and T. Tunaal, Panel on Delayed Fission Neutrons, Proc. IAEA, Vienna (1967), p. 35.
43. G. R. Keepin, J. Nucl. Energy, 7, 13 (1958).
44. Nuclear Data Sheets (1959-1965), or Nuclear Data, Section B (1966-1967), Academic Press, New York and London.
45. J. Wing and P. Fong, Phys. Rev., 136, B.923 (1964).
46. J. Wing and J. D. Varley, Argonne National Laboratory Report, ANL-6886 (1964).
47. G. A. Cowan and C. J. Orth, Proc. UN Intern. Conf. Peaceful Uses At. Energy, 2nd, Geneva, 1958, 7, 328 (1958).
48. N. C. Chrysochoides et al., Panel on Delayed Fission Neutrons, Proc. IAEA, Vienna (1967), p. 213.

#### APPENDIX: CONVOLUTION OF MASS-YIELD DISTRIBUTION

To compare the rates measured at the separator focus with absolute yields, one must either separate the measured curves into single yields considering the resolution function of the apparatus, or convolute the known yields with the resolution function. We chose the second method and illustrate it for the example of fission rate.

In all mass-separator measurements, one basically measures a counting rate at the focus as a function of the magnetic field, B. We examine first a known magnetic field,  $B_0$ , in which ions of mass number  $A_0$  pass through the separator's magnetic field in a stable orbit with radius of curvature,  $\rho_0$ . Because of the moderate resolution, not only fission products of the stable mass  $A_0$ , but rather a mass mixture composed of contributions by neighboring masses is detected at the focus. The following sketch illustrates the situation for two neighboring masses. The x-axis runs from the focus normal to the stable orbit, and in the deflection plane. We want to know the sum of all contributions (cross-hatched areas) to the fission rate,

$\Delta N$ , in the interval  $\Delta x_0$  determined by the fission-product detector. Then the variable  $\frac{\Delta N}{\Delta x_0}$  corresponds to the rate measured at the mass separator.

The computation is performed with the following conditions:

1. The general relationship  $x = x(\rho)$ , determined by the ion optics of the system, is developed for  $\rho = \rho_0$ . To first approximation, a change in the radius of curvature

$$\rho = \rho_0 + \Delta\rho \quad \Delta\rho \ll \rho$$

and the corresponding change in x

$$x = x_0 + \Delta x$$

are related by:

$$\Delta x = C_\rho \cdot \Delta\rho \quad (A1)$$

2. For a known mass number, A, we have

$$(B\rho)_A = \text{const} = f(A). \quad (A2)$$

The values of  $f(A)$  can be obtained from the mass-calibration curve (Fig. 3a). From Eq. (A2) it follows that

$$\left. \frac{\Delta B}{B} \right|_{\rho, A = \text{const}} = \left. \frac{\Delta\rho}{\rho} \right|_{B, A = \text{const}} \quad \text{from Eq. (A2)} \quad \text{from Eq. (A1)} \quad (A3)$$

$$\left. \frac{\Delta x}{x} \right|_{B, A = \text{const}}$$

3. Of the variables in Eq. (A3),

$\Delta B/B$   $_{\rho, A = \text{const}}$  is measured directly (see Sec. 2.3). Measurement shows that this value can be set constant and independent of mass for light and heavy fission products, respectively ((b) Fig. 3 or 4). Thus it follows from Eq. (A3) that

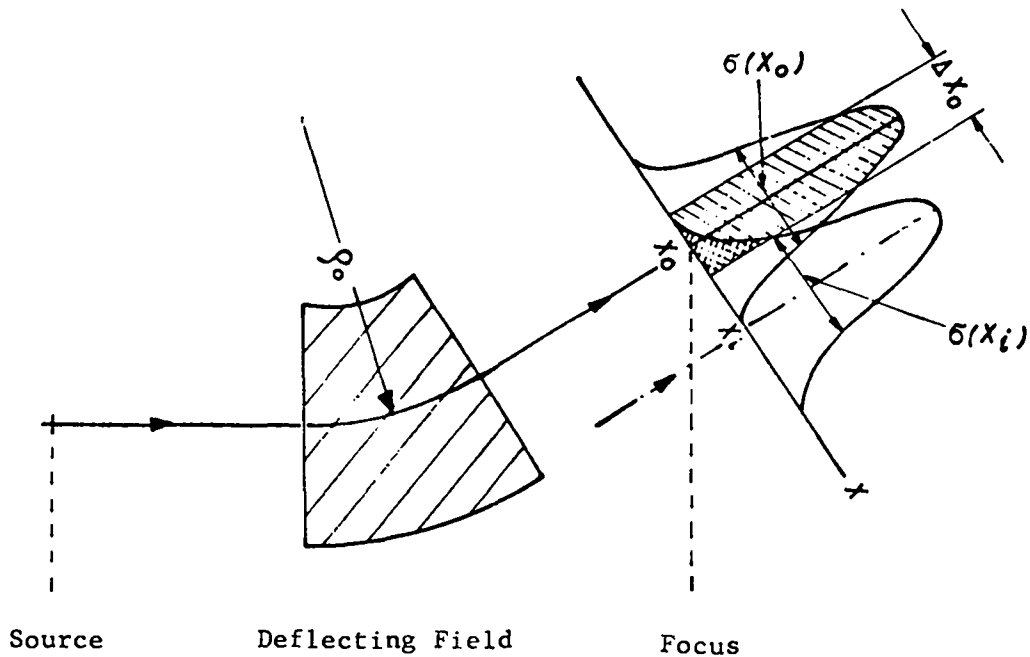
$$\left. \frac{\Delta B}{B} \right|_{\rho, A = \text{const}} = \left. \frac{\Delta x}{x} \right|_{B, A = \text{const}} = \text{const} = R. \quad (A4)$$

The relative resolution capacity, R, for the two mass ranges at the respective optimum helium pressures in the charge-transfer chamber is

$$R = \begin{cases} 4.5\% \text{ for light fission products, } 6.7\text{-Torr He} \\ 6.1\% \text{ for heavy fission products, } 1.4\text{-Torr He} \end{cases}$$

The standard deviation,  $\sigma(x_1)$ , of the resolution function (see sketch) is

$$\sigma(x_1) = \sigma_0 \cdot x_1 \quad (A5)$$



Sketch for Convolution of Mass Yield Distribution.

---


$$\sigma_0 = \frac{R}{2\sqrt{2}n^2} = \begin{cases} 1.6\% \text{ for light fission products, 6.7-Torr He} \\ 6.1\% \text{ for heavy fission products, 1.4-Torr He} \end{cases}$$


---

4. The line configuration is described by a Gaussian curve as a function of the variable  $x$  (see sketch). This assumption is valid provided that the resolution function measured as a function of  $B$  is a Gaussian curve (see Sec. 2.3). In a transformation from  $x$  to  $B$ , the line configuration remains Gaussian.

Using these assumptions, we can represent the fission rate,  $\Delta N$ , passing through the detector window,  $\Delta x_0$ , by:

$$\frac{\Delta N}{\Delta x_0} = K \sum_1 \eta_1 \int_{x_0 - \Delta x_0/2}^{x_0 + \Delta x_0/2} \frac{1}{\sigma(x_1)} \exp - \left\{ (x_1 - x_0)^2 / 2\sigma(x_1)^2 \right\} dx \quad , \quad (A6)$$

where  $\eta_1$  are the mass yields originally given in fission and the proportionality constant  $K$  accounts for the source strength, the solid angle covered by the apparatus, and losses from multiple scattering.

Although the terms  $x_i$  in Eq. (A6) are unknown, the magnetic-field values,  $B_i$ , corresponding to known  $A_i$  can be determined from the measured mass-calibration curve. Therefore, Eq. (A6) is transformed from  $x$  to  $B$  by use of the relationships

$$\sigma(x_i) \longrightarrow \sigma_0 \frac{B_i}{B_0}$$

and

$$(x_i - x_0) \longrightarrow \frac{B_0 - B_i}{B_0}$$


---

Considering finally that the integration over the detector integral for  $\Delta x_0 < \sigma_0 x_0$  can be approximated by the value of the resolution function at the location  $x_0$  or  $B_0$ . Eq. (A6) becomes

$$\frac{\Delta N}{\Delta x_0} = K \sum_i \eta_i \frac{B_0}{\sigma_0 B_i} \exp - \left[ \frac{(B_0 - B_i)^2}{2(\sigma_0 B_i)^2} \right]. \quad (A7)$$

The average mass,  $\bar{A}$ , of the mass mixture present at the focus is

$$\bar{A} = \frac{\sum_i A_i \eta_i \frac{B_0}{\sigma_0 B_i} \exp - \left[ \frac{(B_0 - B_i)^2}{2(\sigma_0 B_i)^2} \right]}{\sum_i \eta_i \frac{B_0}{\sigma_0 B_i} \exp - \left[ \frac{(B_0 - B_i)^2}{2(\sigma_0 B_i)^2} \right]}. \quad (A8)$$

To determine the fission-product mass distribution, the rate is measured at the fission-product detector focus as a function of the magnetic field.

The measured rates may, in each instance, be compared with the  $\frac{\Delta N}{\Delta x_0}$  computed from Eq. (A7).

For constant  $\Delta x_0$ , both the measured and computed rates are defined. This condition corresponds to a  $\Delta B$  window increasing proportionally to  $B$ , so that the curves plotted against  $B$  are distorted. The true shape, that related to a constant  $\Delta B$  interval, of the distribution plotted against  $B$  is obtained by  $\frac{1}{B}$  correction of the distribution ("distortion correction").